Studies on the mechanism of ciliary protein localization and the molecular basis of ciliopathies

2021

Hantian Qiu

TABLE OF CONTENTS

GENERAL INTRODUCTION

Cilia are microtubule-based hair-like organelles that project from the cell surface of almost all cell types of the human body. The ciliary membrane contains specific receptors and ion channels that sense and transduce extracellular chemical and physical signals, such as fluid flow and light, sonic hedgehog and growth factors (Briscoe and Thérond, 2013; Mukhopadhyay and Rohatgi, 2014). Owing to their crucial roles, defects in cilia cause a variety of genetic disorders collectively referred to as the ciliopathies, including Joubert syndrome (JBTS), short-rib thoracic dysplasia (SRTD), Meckel syndrome (MKS), Bardet-Biedl syndrome (BBS), and nephronophthisis. Ciliopathies usually are accompanied with a variety of clinical manifestations, such as hydrocephalus, infertility, airway diseases, morbid obesity, skeletal and brain malformations, polycystic diseases of the kidney, liver and pancreas, as well as retinal diseases and defects of hearing and smell, (Braun and Hildebrandt, 2017; Madhivanan and Aguilar, 2014).

Accumulating lines of evidence indicate that compositions of proteins within cilia those of proteins and lipids on the ciliary membrane are distinguished from those in the cell body and on the plasma membrane, respectively. Various soluble and membrane proteins, such as G protein–coupled receptors (GPCRs), are specifically present within cilia and on the ciliary membrane. Therefore, assembly of cilia and the maintenance of ciliary functions strictly rely on the proper trafficking of these proteins, which is mediated by the intraflagellar transport (IFT) machinery, often referred to as IFT trains or IFT particles (Ishikawa and Marshall, 2011; Rosenbaum and Witman, 2002; Sung and Leroux, 2013). The IFT machinery is comprised of the IFT-A and IFT-B complexes. Studies have found that the IFT-B complex mediates anterograde protein trafficking from the ciliary base to the tip powered by kinesin-2 motor proteins, whereas the IFT-A complex mediates retrograde trafficking with the aid of the dynein-2 complex. In addition, the BBSome serves as a connector between the IFT machinery and ciliary membrane proteins (Figs. 0-1 and 0-2) (Ishikawa and Marshall, 2011; Nakayama and Katoh, 2018; Sung and Leroux, 2013; Taschner and Lorentzen, 2016).

Although cilia play a crucial role in the human body, the components involved in cilia-specific functions and the molecular mechanisms underlying the various ciliopathies are poorly understood. The research of functional role and subcellular localization of ciliary proteins is therefore necessary for a better understanding of cilia-related disorder, and the identification of molecular basis of ciliopathies can be also helpful to develop novel therapeutic strategies.

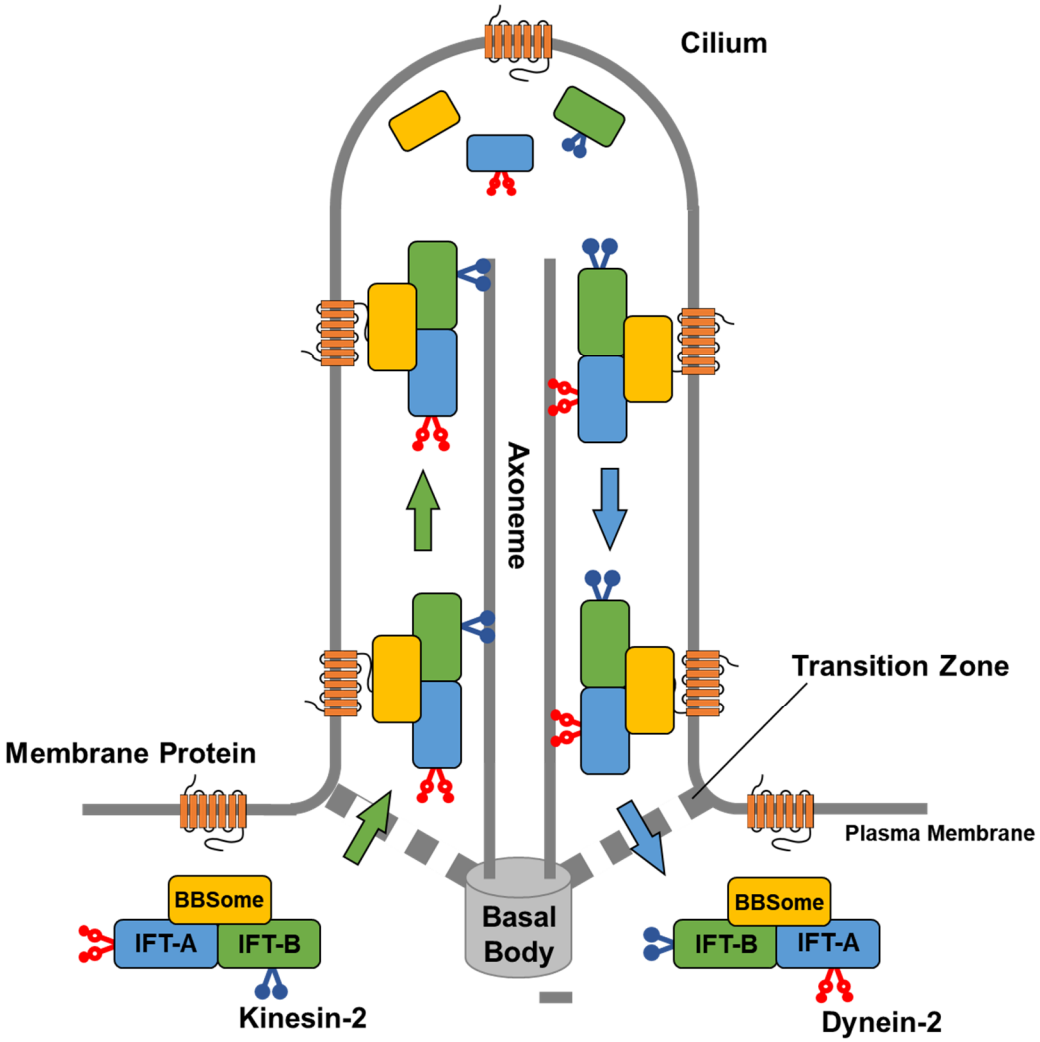

Fig. 0-1. Schematic illustration of ciliary protein trafficking mediated by the IFT machinery and the BBSome

Cilia are the microtubule-based structures projecting from the surface of most eukaryotic cells. Bidirectional trafficking of ciliary proteins along the axonemal microtubules is mediated by the IFT machinery composed of the multisubunit complexes (IFT-A, IFT-B, and BBSome) and the kinesin-2 and dynein-2 motor complexes. The IFT particles are assembled around the basal body, enter the cilium across the transition zone (TZ), and undergo processive anterograde trafficking along the axoneme powered by kinesin-2. At the ciliary tip, the IFT particles are thought to once disassemble to release cargo proteins. The IFT particles are then reassembled and cargos are loaded, and the assembled particles undergo retrograde trafficking powered by dynein-2. The particles exit the cilium across the TZ.

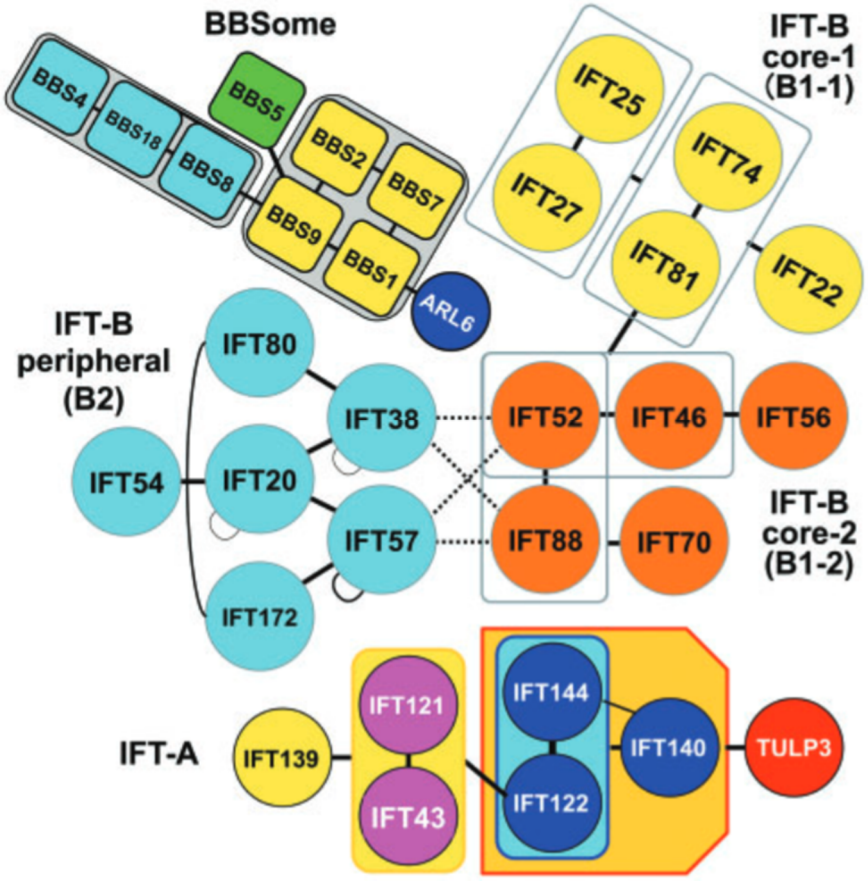

Fig. 0-2. Architectures of the IFT-A, IFT-B and BBSome complexes

Architectures of the IFT-A, IFT-B and BBSome complexes predicted from previous studies of our research group (Katoh et al., 2015; Hirano et al., 2017; Nakayama and Katoh, 2018). IFT-A, IFT-B and BBSome are multisubunit complexes composed of 6, 16 and 8 subunits, respectively. The IFT-A complex can be divided into the core subcomplex composed of IFT122/140/144, which interacts with the TULP3 adaptor, and the non-core subcomplex composed of IFT43/121/139. The IFT-B complex can be divided into the core and peripheral subcomplexes, that are composed of 10 subunits (IFT22/25/27/46/52/56/70/74/81/88) and six subunits (IFT20/38/54/57/80/172), respectively. These subcomplexes are linked by composite interactions involving the connecting tetramer composed of IFT38/52/57/88. The BBSome complex can be divided into the linker subcomplex composed of BBS4/8/18, and the core subcomplex composed of BBS1/2/7/9. BBS9 serves as a hub subunit that connects the linker and core subcomplexes and binds BBS5.

ABBREVIATIONS

Ac-tubulin	acetylated α-tubulin
ANOVA	analysis of variance
ARL	Arf-like
BBS	Bardet-Biedl syndrome
Cas	CRISPR-associated protein
CC	coiled-coil
cDNA	complementary DNA
CED	cranioectodermal dysplasia
CID	chemically inducible dimerization
CRISPR	clustered regularly interspaced short palindromic repeat
CTS	ciliary targeting sequence
DNA	deoxyribonucleic acid
DTT	dithiothreitol
EDTA	ethylenediaminetetraacetic acid
EGFP	enhanced green fluorescent protein
EvC	Ellis-van Creveld syndrome
FBS	fetal bovine serum
FKBP	FK506-binding protein
FOP	FGFR1 oncogene partner
FRB	FKBP–rapamycin-binding domain
GEF	guanine nucleotide exchange factor
GFP	green fluorescent protein
GPCR	G protein–coupled receptor
GST	glutathione S-transferase
GTP	guanosine triphosphate
HEK	human embryonic kidney
HEPES	4-(2-hydroxyethyl)-1-piperazineethanesulfonic acid
Hh	Hedgehog
hTERT	human telomerase reverse transcriptase
IFT	intraflagellar transport
JATD	Jeune asphyxiating thoracic dystrophy
JBTS	Joubert syndrome
KO	knockout
LIC	light intermediate chain
mChe	mCherry
MKS	Meckel syndrome
Nb	nanobody
NN-CH	divergent calponin homology domain

PAM	proto-spacer adaptor motif
PCR	polymerase chain reaction
RFP	red fluorescent protein
RNA	ribonucleic acid
RPE	retinal pigment epithelial
SAG	Smoothened Agonist
SD	standard deviation
SDS-PAGE	sodium dodecyl sulfate-polyacrylamide gel electrophoresis
sgRNA	single guide RNA
SMO	Smoothened
SRPS	short rib-polydactyly syndrome
SRTD	short-rib thoracic dysplasia
SSTR	somatostatin receptor
tBFP	TagBFP
tRFP	TagRFP
TULP	Tubby-like protein
TZ	transition zone
VIP	visible immunoprecipitation
WT	wild type

Chapter 1: The mechanism of the localization of INPP5E to the ciliary membrane

ABSTRACT

Compositions of proteins and lipids within cilia and on the ciliary membrane are maintained to be distinct from those of the cytoplasm and plasma membrane, respectively, by the presence of the ciliary gate. INPP5E is a phosphoinositide 5-phosphatase that is localized on the ciliary membrane by anchorage via its C-terminal prenyl moiety. In addition, the ciliary membrane localization of INPP5E is determined by the small GTPase ARL13B. However, it remained unclear as to how ARL13B participates in the localization of INPP5E. I here show that wild-type INPP5E, INPP5E(WT), in *ARL13B*-knockout cells and an INPP5E mutant defective in ARL13B binding, INPP5E(ΔCTS), in control cells were unable to show steady-state localization on the ciliary membrane. However, not only INPP5E(WT) but also INPP5E(ΔCTS) was able to rescue the abnormal localization of ciliary proteins in *INPP5E*-knockout cells. Analysis using the chemically induced dimerization system demonstrated that INPP5E(WT) in *ARL13B*-knockout cells and INPP5E(ΔCTS) in control cells were able to enter cilia, but neither was retained on the ciliary membrane due to the lack of the INPP5E–ARL13B interaction. Thus, the data presented here demonstrate that binding of INPP5E to ARL13B is essential for its steady-state localization on the ciliary membrane but is dispensable for its entry into cilia.

INTRODUCTION

Primary cilia are sensory organelles for extracellular mechanical stimuli, such as fluid flow, and for signaling molecules, such as the Hedgehog (Hh) morphogen (Bangs and Anderson, 2017; Gigante and Caspary, 2020). To achieve their function of receiving specific signals, the composition of proteins and lipids of the ciliary membrane and ciliary interior are distinguished from those of the contiguous plasma membrane and cytoplasm, respectively. This distinction relies on the presence of the ciliary gate, which is composed of transition fibers (TFs) of the basal body and the transition zone (TZ) at the ciliary base (Garcia-Gonzalo and Reiter, 2017; Gonçalves and Pelletier, 2017).

The TZ restricts entry and exit of ciliary proteins (Nachury and Mick, 2019), and acts as a diffusion barrier for membrane proteins and lipids between the ciliary and plasma membranes (Jensen and Leroux, 2017), and as a permeability barrier for soluble proteins (Takao and Verhey, 2016). Transport of proteins within cilia and across the ciliary gate is mediated by the intraflagellar transport (IFT) machinery composed of multisubunit complexes (Nakayama and Katoh, 2020; Taschner and Lorentzen, 2016). In addition to the role of the IFT-A complex and the TULP3 adaptor protein in retrograde ciliary protein trafficking powered by dynein-2, these molecules mediate the import of ciliary membrane proteins across the ciliary gate (Badgandi et al., 2017; Hirano et al., 2017; Kobayashi et al., 2021; Mukhopadhyay et al., 2010; Park et al., 2013). On the other hand, the IFT-B complex mediates anterograde ciliary protein trafficking powered by kinesin-2 and the export of ciliary membrane proteins coupled with the BBSome (Eguether et al., 2014; Lechtreck et al., 2013; Liew et al., 2014; Liu and Lechtreck, 2018; Nozaki et al., 2019; Nozaki et al., 2018; Ye et al., 2018). Owing to the importance of the IFT machinery and the TZ for the integrity of cilia, a broad spectrum of hereditary disorders, collectively referred to as the ciliopathies, arise from mutations in the genes of IFT and TZ components (Braun and Hildebrandt, 2017; Reiter and Leroux, 2017).

The targeting of lipidated membrane proteins, such as C-terminally prenylated INPP5E, to the ciliary membrane is mediated by a distinct system (Jensen and Leroux, 2017; Stephen and Ismail, 2016). C-terminally prenylated and N-terminally myristoylated membrane proteins are first trapped in the cytosol by PDE6D and UNC119, respectively, both of which are RhoGDI-like solubilizing factors for lipidated proteins (Stephen and Ismail, 2016). The release of bound PDE6D and UNC119 from lipidated proteins is stimulated by allosteric binding of the ARL3 GTPase (Fansa and Wittinghofer, 2016; Fisher et al., 2020; Ismail et al., 2011).

A distinct phosphoinositide distribution is maintained on the ciliary membrane, and

a key regulator is INPP5E, which hydrolyzes the 5-phosphate of PtdIns(4,5)P_2 and PtdIns(3,4,5)P_3 (Conduit and Vanhaesebroeck, 2020). Particularly, owing to the presence of ciliary INPP5E, PtdIns(4)P is enriched in the ciliary membrane, whereas PtdIns(4,5)P_2 is limited to the ciliary base (Chávez et al., 2015; Garcia-Gonzalo et al., 2015; Nakatsu, 2015). The physiological relevance of the PtdIns(4)P-rich conditions on the ciliary membrane might be associated with the function of TULP3, which acts as an adaptor connecting the IFT-A complex with ciliary membrane proteins (Badgandi et al., 2017; Mukhopadhyay et al., 2010). As the Tubby domain of TULP3 binds to PtdIns(4,5)P_2, retrograde ciliary protein trafficking mediated by IFT-A and TULP3 is impaired in the absence of ciliary INPP5E, namely under ciliary PtdIns(4,5)P_2-rich conditions. Thus, in cells derived from *Inpp5e*-knockout (KO) mice, the aberrant accumulation of GPR161, which is a negative regulator of Hh signaling, was observed (Chávez et al., 2015; Garcia-Gonzalo et al., 2015), and release of extracellular vesicles from the ciliary tip was promoted (Phua et al., 2017). On the other hand, another study indicated that hydrolysis of PtdIns(3,4,5)P_3 by INPP5E at the ciliary base is important for the convergent regulation of Hh and phosphoinositide signaling (Dyson et al., 2017).

INPP5E has a C-terminal CaaX motif for prenylation, and its localization to the ciliary membrane is therefore under the regulation of ARL3 via PDE6D (Fansa et al., 2016; Humbert et al., 2012). In addition, INPP5E has a ciliary targeting sequence (CTS), F^{609}DRELYL^{615}, to which another small GTPase, ARL13B, binds (Humbert et al., 2012); namely, ARL13B directly determines the ciliary membrane targeting of INPP5E (Humbert et al., 2012; Nozaki et al., 2017). On the other hand, ARL13B was reported to act as a guanine nucleotide exchange factor (GEF) for ARL3 (Gotthardt et al., 2015; Ivanova et al., 2017; Zhang et al., 2016). Thus, it is also possible that ARL13B indirectly regulates the ciliary targeting of INPP5E via stimulating the ARL3-mediated release of PDE6D from INPP5E (Stephen and Ismail, 2016). In this context, it is notable that mutations in the genes of all the components involved in the ciliary targeting of INPP5E are known to cause JBTS, namely, INPP5E/JBTS1, ARL13B/JBTS8, PDE6D/JBTS22, and ARL3/JBTS35 (Parisi and Glass, 2003 [updated 2017]).

In Chapter 1, I therefore analyzed how the ciliary localization of INPP5E is determined. Unexpectedly, a stably expressed INPP5E construct lacking the CTS was able to partially restore the normal localization of ciliary proteins in *INPP5E*-KO cells, even though the steady-state localization of the INPP5E construct to the ciliary membrane was not detectable. I eventually found that an INPP5E mutant lacking the CTS is able to transiently enter cilia but is unable to be retained on the ciliary membrane owing to impaired ARL13B binding.

RESULTS

INPP5E-KO and ARL13B-KO cells show similar phenotypes

Our research group previously established *ARL13B*-KO cell lines from human telomerase reverse transcriptase-immortalized retinal pigment epithelial 1 (hTERT-RPE1) cells and analyzed their phenotypes, including the targeting of INPP5E to the ciliary membrane (Nozaki et al., 2017). On the other hand, previous studies on the cellular functions of INPP5E were performed using mouse embryonic fibroblasts (MEFs) from *Inpp5e*-KO mice, although these mice themselves were embryonic lethal (Chávez et al., 2015; Dyson et al., 2017; Garcia-Gonzalo et al., 2015; Phua et al., 2017). To directly compare the effects of the absence of ARL13B and INPP5E in the same cell background, I established INPP5E-KO cell lines from hTERT-RPE1 cells.

Two independent KO cell lines (#INPP5E-2-2 and #INPP5E-2-19) (Fig. 1-1) were used for the following analyses. In these *INPP5E*-KO cell lines, the ciliary localization of INPP5E was abolished (Fig. 1-2, B, C), whereas ARL13B was retained on the ciliary membrane (Fig. 1-2, F, G). Ciliary INPP5E signals were also absent in *ARL13B*-KO cells (Fig. 1-2D), as described previously (Nozaki et al., 2017). These observations are consistent with the fact that ciliary membrane localization of INPP5E is dependent on ARL13B.

I then analyzed the localization of the IFT-B and IFT-A proteins in INPP5E-KO and ARL13B-KO cells. In a previous study (Nozaki et al., 2017), our research group showed that in ARL13B-KO cells, there is a tendency of IFT88 (an IFT-B subunit), IFT140 (an IFT-A subunit), and TULP3, which is an adaptor protein connecting the IFT-A complex with PtdIns(4,5)P_2 on the ciliary membrane, to accumulate at the ciliary tip (Mukhopadhyay et al., 2010). In control RPE1 cells, most IFT88 was found around the ciliary base, with a small proportion at the distal tip (Fig. 1-3A; also see Fig. 1-3M); in this context, it is notable that a recent super-resolution imaging study of our research group showed the localization of IFT88 at the TFs and in the TZ (Katoh et al., 2020). By contrast, the proportion of IFT88 found at both the ciliary base and tip and the total amount of IFT88 within cilia were significantly increased in *ARL13B*-KO cells (Fig. 1-3D), as described previously, and in *INPP5E*-KO cells (Fig. 1-3, B, C; also see Fig. 1-3, M, P).

IFT140 was also mainly found at the ciliary base in control RPE1 cells (Fig. 1-3E), and at both the base and tip in *ARL13B*-KO cells (Fig. 1-3H; also see Fig. 1-3N), as described previously. In *INPP5E*-KO cells, IFT140 was more broadly distributed within cilia (Fig. 1-3, F and G; also see Fig. 1-3, N, Q), consistent with a previous study using

MEFs from *Inpp5e*-KO mice (Garcia-Gonzalo et al., 2015). EGFP-TULP3 was found mainly around the ciliary base in control cells (Fig. 1-3I), whereas it was found throughout the entire cilia in *INPP5*E-KO and *ARL13B*-KO cells, resulting in an increase in the total ciliary EGFP-TULP3 level (Fig. 1-3, J–L; also see Fig. 1-3, O, R). These observations are consistent with the notions that the IFT-A adaptor TULP3 binds to PtdIns(4,5)P_2 (Mukhopadhyay et al., 2010), and that the increased level of PtdIns(4,5)P_2 caused by INPP5E deficiency on the ciliary membrane results in the ciliary retention of the IFT machinery via the binding of TULP3 to PtdIns(4,5)P_2.

I then compared the localization of two GPCRs, GPR161 and Smoothened (SMO), in control, *INPP5E*-KO, and *ARL13*B-KO cells. GPR161 and SMO are class A and class F GPCRs, and are negative and positive regulators of Hh signaling, respectively; upon activation of Hh signaling, GPR161 exit cilia, whereas SMO enters cilia (Gigante and Caspary, 2020; Mukhopadhyay and Rohatgi, 2014; Nachury and Mick, 2019). In control RPE1 cells, GPR161 was evenly distributed on the ciliary membrane under basal conditions (Fig. 1-4A), whereas the majority of GPR161 exited cilia when the cells were stimulated with Smoothened Agonist (SAG) (Fig. 1-4E; also see Fig. 1-4, Q, S). In striking contrast, GPR161 was retained on the ciliary membrane in *INPP5E*-KO and *ARL13*B-KO cells, even upon stimulation with SAG (compare Fig. 1-4, F–H with B–D; also see Fig. 1-4, Q, S). Thus, as in the absence of ARL13B (Nozaki et al., 2017), the exit of GPR161 from cilia is suppressed upon SAG stimulation in *INPP5E*-KO cells.

On the other hand, in control RPE1 cells, SMO was not found within cilia before SAG treatment (Fig. 1-4I), and entered cilia upon the stimulation of cells with SAG (Fig. 1-4M; also see Fig. 1-4R). In *INPP5E*-KO and *ARL13B*-KO cells, SMO was also absent from cilia under basal conditions (Fig. 1-4, J–L), and entered cilia upon SAG treatment (Fig. 1-4, N–P; also see Fig. 1-4, R, T), similarly to control RPE1 cells. However, the ciliary entry of SMO was not significantly affected by the absence of INPP5E; the data showing that SMO localization was not affected in the absence of INPP5E is consistent with a previous study, probably due to the participation of TULP3 in the ciliary trafficking of class A GPCRs but not that of SMO, which is a class F GPCR (Badgandi et al., 2017; Garcia-Gonzalo et al., 2015).

Steady-state ciliary localization of INPP5E is not crucial for its role as a modulator of ciliary function

I then analyzed whether the abnormal phenotypes of *INPP5E*-KO cells can be rescued by the stable expression of INPP5E constructs (see Fig. 1-5A). As shown in Fig. 1-5, the stable expression of EGFP-INPP5E(WT) restored the normal localization of

IFT88 and IFT140; namely, mainly at the ciliary base (compare panels C and G with B and F, respectively; also see Fig. 1-5, J, K). On the other hand, the expression of EGFP-fused INPP5E(D477N), in which the Asp residue that is crucial for phosphatase activity is substituted to Asn (Bielas et al., 2009; Kong et al., 2006), did not restore the localization of IFT88 or IFT140, even though this mutant itself was able to localize within cilia (Fig. 1-5, D, H), indicating that the phosphatase activity is essential for INPP5E function. Somewhat unexpected was that when EGFP-fused INPP5E(ΔCTS) was expressed in *INPP5E*-KO cells; the localization of IFT88 and IFT140 were partially but significantly restored, although the INPP5E mutant itself was undetectable within cilia (Fig. 1-5, E, I; also see Fig. 1-5, J, K). The INPP5E(ΔCTS) mutant lacks the FDRELYL sequence, to which ARL13B binds (Humbert et al., 2012). I confirmed the binding of ARL13B to INPP5E(WT) but not to the INPP5E(ΔCTS) construct by the visible immunoprecipitation (VIP) assay (Fig. 1-5L) and by subsequent immunoblotting analysis (Fig. 1-5M).

I also analyzed the effects of stable expression of the INPP5E constructs on the GPR161 localization of *INPP5E*-KO cells. The stable expression of EGFP-INPP5E(WT), but not EGFP-INPP5E(D477N), eliminated the retention of GPR161 within cilia after SAG treatment (Fig. 1-6, F, G). On the other hand, the stable expression of EGFP-INPP5E(ΔCTS) partially but significantly rescued the ciliary accumulation of GPR161 upon SAG treatment (Fig. 1-6, H; also see Fig. 1-6I). Thus, the abnormal phenotypes of *INPP5E*-KO cells appeared to be rescued by the exogenous expression of not only INPP5E(WT) but also the INPP5E construct with compromised ability to target to the ciliary membrane, at least in the steady state.

The CTS of INPP5E is required for its ciliary retention but is dispensable for its entry into cilia

I then investigated the mechanism as to how INPP5E(ΔCTS) partially rescued the defects of *INPP5E*-KO cells, even though the INPP5E construct itself was not detectable within cilia. To this end, I expressed the INPP5E constructs in *ARL13B*-KO cells to analyze whether they were able to rescue the defects of *ARL13B*-KO cells. As expected from the delocalization of endogenous INPP5E in *ARL13B*-KO cells (see Fig. 1-2D), the ciliary localization of exogenously expressed EGFP-INPP5E(WT) and EGFP-INPP5E(D477N) was barely detectable (Fig. 1-7, B, F, and C, G, respectively). However, EGFP-INPP5E(WT) was able to restore the localization of IFT88 and IFT140 predominantly at the ciliary base in *ARL13B*-KO cells (Fig. 1-7, B, F; also see Fig. 1-7, I, J). Furthermore, the normal localization of IFT88 and IFT140 was also significantly restored by the exogenous expression of EGFP-INPP5E(ΔCTS) (Fig. 1-7, D, H; also see

Fig. 1-7, I, J).

The absence of INPP5E(ΔCTS) in *INPP5E*-KO cells and INPP5E(WT) in *ARL13B*-KO cells suggests the possibility that INPP5E can modulate ciliary functions outside of cilia. In this context, it is interesting to note the study of Dyson et al. using MEFs from *Inpp5e*-KO mice, in which the authors proposed that INPP5E regulates the molecular organization of the TZ on the basis of their data that TZ proteins were delocalized from the TZ upon treatment of *Inpp5e*-KO MEFs with SAG (Dyson et al., 2017). On the other hand, our research group recently showed that in KO cells of MKS1 or B9D2, which are components of the MKS module of the TZ (Garcia-Gonzalo and Reiter, 2017), ciliary transmembrane and lipid-anchored membrane proteins, including GPR161, SMO, ARL13B, and INPP5E, are delocalized from cilia irrespective of SAG treatment (Okazaki et al., 2020), and this was due to the disruption of the TZ that acts as a diffusion barrier between the ciliary and plasma membranes.

I therefore analyzed the integrity of the TZ in *INPP5E*-KO and *ARL13B*-KO cells. As shown in Fig. 1-8, A–H, signals for TCTN1, a MKS component of the TZ, were detected at the ciliary base in control RPE1, *INPP5E*-KO, and *ARL13B*-KO cells under both basal (–SAG) and SAG-stimulated (+SAG) conditions [note that I used an anti-TCTN1 antibody from the same commercial source as that used by Dyson et al. (2017)]. I also analyzed the localization of stably expressed EGFP-MKS1, and found that its TZ localization was not changed by SAG treatment in control RPE1, INPP5E-KO, and ARL13B-KO cells (Fig. 1-8, I–P) [note that the EGFP-MKS1 construct was previously confirmed to rescue the delocalization of ciliary membrane proteins when expressed in *MKS1*-KO cells (Okazaki et al., 2020)]. Thus, my attempts to reproduce the observations of Dyson et al. were unsuccessful. I do not know the exact reason for the apparent discrepancy, but it might be a result of the cells used; i.e., MEFs from *Inpp5e*-KO mice in the study by Dyson et al. and *INPP5E*-KO RPE1 cells in the present study.

On the basis of the results shown in Figs. 1-6 and 7, it is possible that in the absence of the INPP5E–ARL13B interaction, INPP5E is still able to enter cilia but is unable to be retained on the ciliary membrane. To address this possibility, I utilized the chemically inducible dimerization (CID) system (Komatsu et al., 2010; Lin et al., 2013; Takada et al., 2018) to enable trapping of the INPP5E constructs onto the ciliary membrane, controlled by rapamycin (schematically shown in Fig. 1-9A). I first established control RPE1, *INPP5E*-KO, and *ARL13B*-KO cells stably expressing the SSTR3-mChe-FRB construct, in which mCherry (mChe) and the FK506-binding protein (FKBP)–rapamycin-binding domain (FRB) were fused to the C-terminus of SSTR3, a GPCR constitutively localized on the ciliary membrane (Berbari et al., 2008). Then, N-terminally FKBP-EGFP-fused

INPP5E constructs were expressed in the SSTR3-mChe-FRB–expressing cells. In the absence of rapamycin, FKBP-EGFP-INPP5E(ΔCTS) in control RPE1 and *INPP5E*-KO cells and FKBP-EGFP-INPP5E(WT) in *ARL13B*-KO cells were not found within cilia (Fig. 1-9, B, F, and H). However, after the addition of rapamycin (final concentration: 200 nM) for 15 min, all the INPP5E constructs were observed within cilia (Fig. 1-9, C, G, and I). As a negative control, EGFP-INPP5E(ΔCTS), which lacks the FKBP sequence, did not undergo rapamycin-induced entry into cilia in control RPE1 cells expressing SSTR3-mChe-FRB (Fig. 1-9, D and E). These observations altogether indicate that INPP5E is able to move in and out of cilia across the ciliary gate even in the absence of its binding to ARL13B via its CTS, and even in the absence of ARL13B itself, but is unable to be retained on the ciliary membrane due to the lack of the INPP5E–ARL13B interaction.

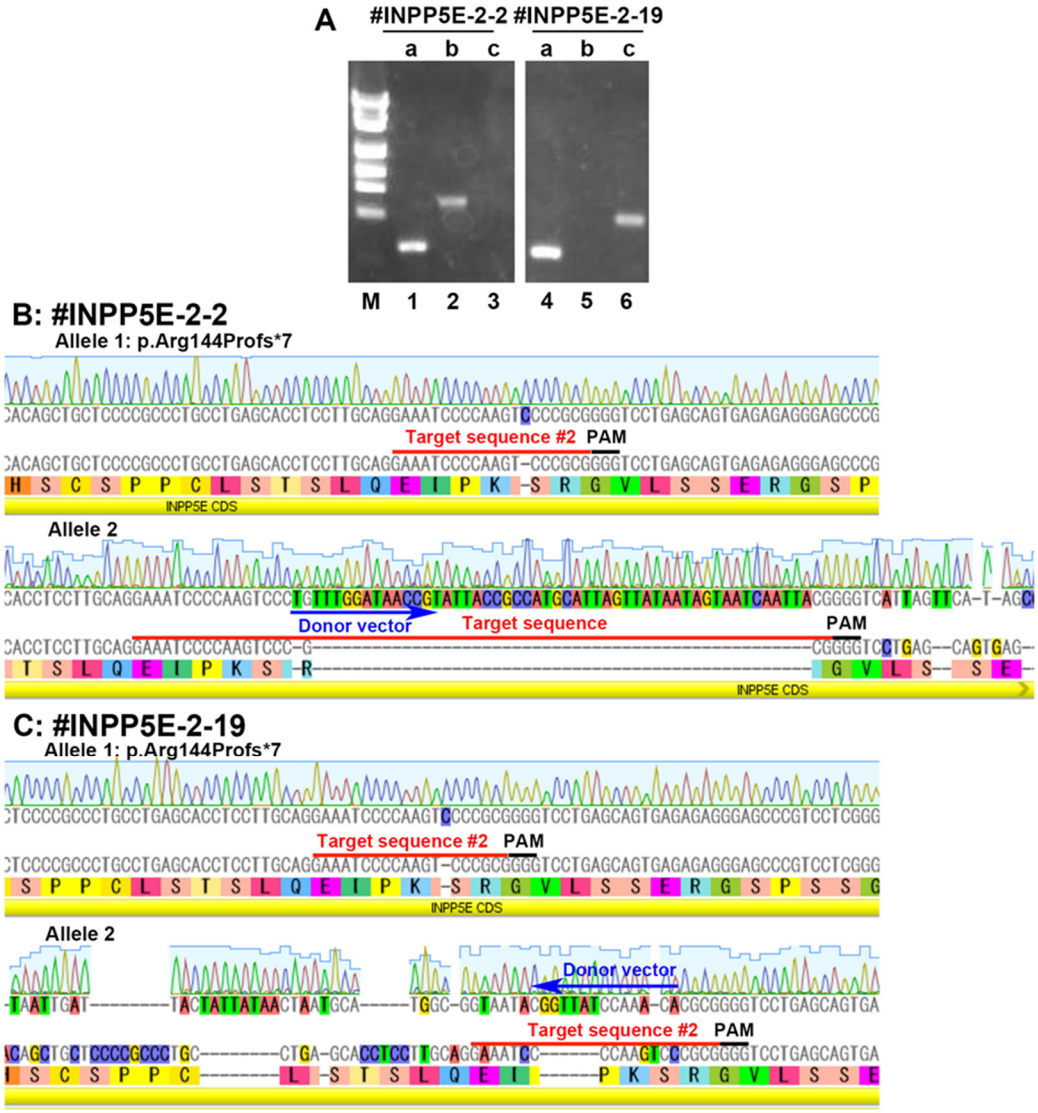

Fig. 1-1. Genomic PCR and sequence analyses of the *INPP5E*-KO cell lines

(A) Genomic DNA extracted from the *INPP5E*-KO cell lines #INPP5E-2-2 and #INPP5E-2-19 were subjected to PCR using the indicated primer sets (see Table S1-3) to detect alleles with a small indel or no insertion (a), or with forward (b) or reverse (c) integration of the donor knock-in vector. M, molecular weight marker (PSU1 DNA ladder). (B, C, E, and F) Alignments of allele sequences of the #INPP5E-2-2 (B) and #INPP5E-2-19 (C) cell lines determined by sequencing of the PCR products shown in (A). Red and black lines indicate the target sequence and PAM sequence, respectively, and blue arrows indicate the direction of integration of the donor knock-in vector.

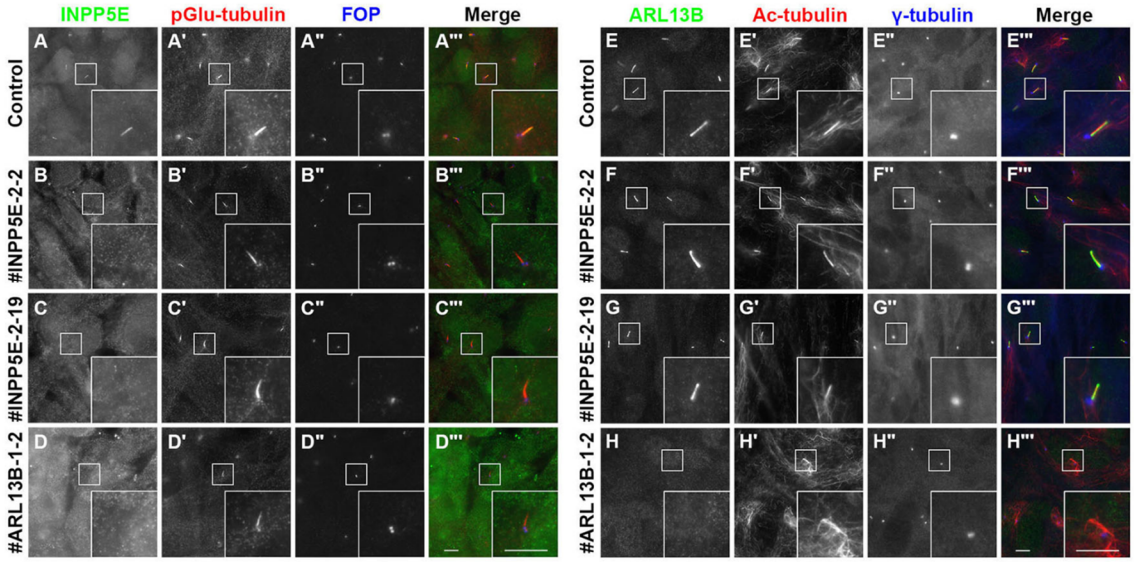

Fig. 1-2. Localization of INPP5E and ARL13B in *INPP5E*-KO and *ARL13B*-KO cells
Control RPE1 cells (A, E), the *INPP5E*-KO cell lines #INPP5E-2-2 (B, F) and #INPP5E-2-19 (C, G), and the *ARL13B*-KO cell line #ARL13B-1-2 (D, H), were serum-starved for 24 h and immunostained with a combination of an anti-INPP5E antibody (A–D), the GT335 antibody that recognizes polyglutamylated (pGlu) tubulin (A′–D′), and an anti-FOP antibody (A″–D″), or antibodies against ARL13B (E–H), acetylated α-tubulin (Ac-tubulin) (E′–H′), and γ-tubulin (E″–H″). Insets are 2.5-fold enlarged images of the boxed regions. Scale bars, 5 μm.

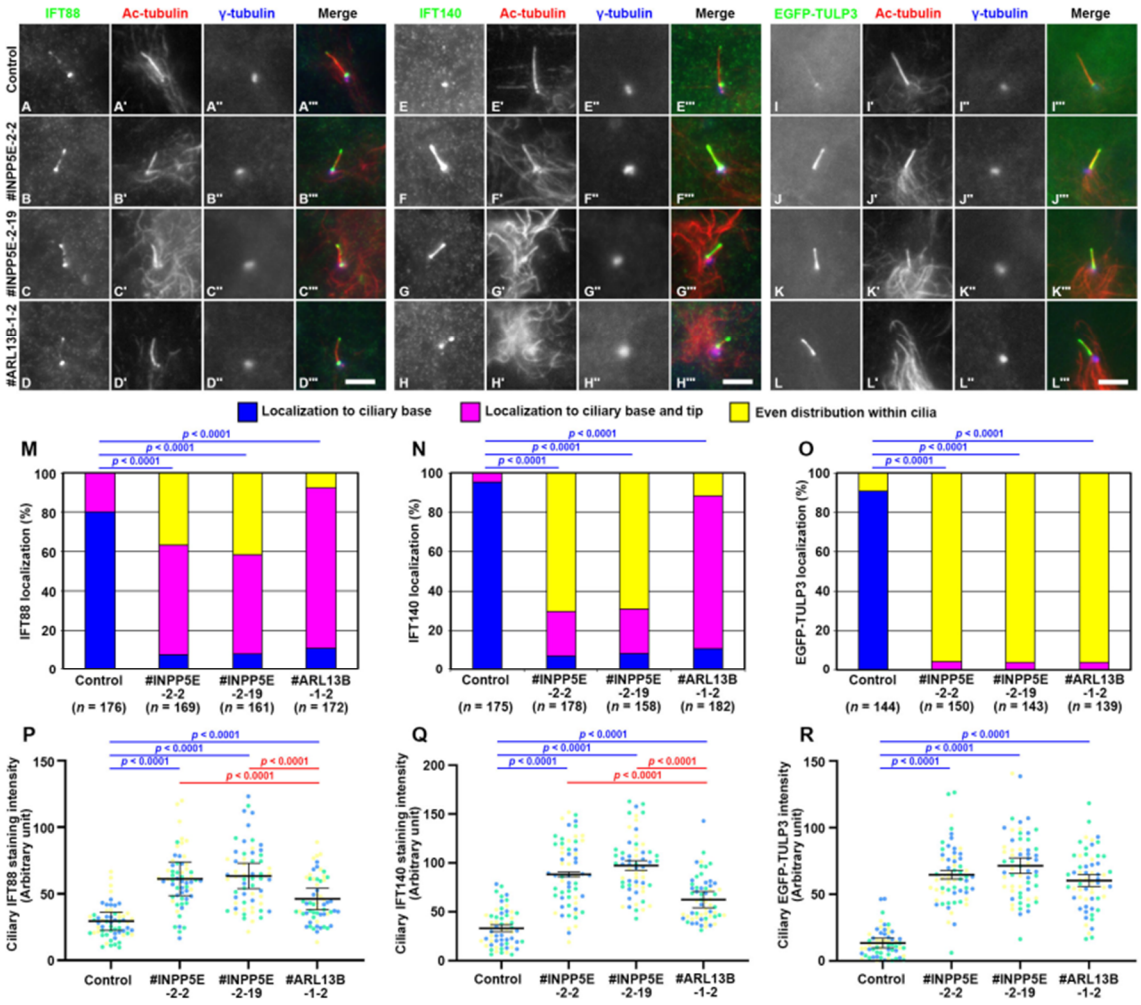
IFT88
Ac-tubulin
γ-tubulin
Merge
IFT140
EGFP-TULP3
Control
#INPP5E-2-2
#INPP5E-2-19
#ARL13B-1-2
Localization to ciliary base
Localization to ciliary base and tip
Even distribution within cilia
M
N
O
IFT88 localization (%)
IFT140 localization (%)
EGFP-TULP3 localization (%)
Control (n = 176)
#INPP5E -2-2 (n = 169)
#INPP5E -2-19 (n = 161)
#ARL13B -1-2 (n = 172)
Control (n = 175)
#INPP5E -2-2 (n = 178)
#INPP5E -2-19 (n = 158)
#ARL13B -1-2 (n = 182)
Control (n = 144)
#INPP5E -2-2 (n = 150)
#INPP5E -2-19 (n = 143)
#ARL13B -1-2 (n = 139)
p < 0.0001
P
Q
R
Ciliary IFT88 staining intensity (Arbitrary unit)
Ciliary IFT140 staining intensity (Arbitrary unit)
Ciliary EGFP-TULP3 intensity (Arbitrary unit)
Control
#INPP5E -2-2
#INPP5E -2-19
#ARL13B -1-2

Fig. 1-3. Accumulation of IFT-A and IFT-B proteins at the ciliary tips of *INPP5E*-KO and *ARL13B*-KO cells

(A–H) Control RPE1 cells (A, E), the *INPP5E*-KO cell lines #INPP5E-2-2 (B, F) and #INPP5E-2-19 (C, G), and the *ARL13B*-KO cell line #ARL13B-1-2 (D, H), were serum-starved for 24 h and triply immunostained for either IFT88 (A–D) or IFT140 (E–H), Ac-tubulin (A′–H′), and γ-tubulin (A″–H″). (I–L) Control RPE1 cells (I), the *INPP5E*-KO cell lines #INPP5E-2-2 (J) and #INPP5E-2-19 (K), and the *ARL13B*-KO cell line #ARL13B-1-2 (L) stably expressing EGFP-TULP3 were serum-starved for 24 h, and immunostained with antibodies against Ac-tubulin (I′–L′) and γ-tubulin (I″–L″). Scale bars, 5 μm. (M–O) Localization of IFT88 (M), IFT140 (N), and EGFP-TULP3 (O) in individual control, *INPP5E*-KO, and *ARL13B*-KO cells was classified as 'localization to ciliary base', 'localization to ciliary base and tip', and 'even distribution throughout cilia', and the number of cells in each category was counted. The percentages of these populations are expressed as stacked bar graphs. Values are means of three independent experiments, and the total numbers of cells analyzed (*n*) are indicated. In each set of experiments, 53 to 62 cells (M), 49 to 63 cells (N), and 43 to 52 cells (O) were analyzed. Statistical significances were calculated for the 'base' category using two-way ANOVA followed by the Tukey multiple comparison test. (P–R) The relative ciliary staining intensities of IFT88 (P) and IFT140 (Q), and the relative ciliary intensities of EGFP-TULP3 (R) in control, *INPP5E*-KO, and *ARL13B*-KO cells were estimated and expressed as scatter plots. Different colored dots represent three independent experiments ($n = 20 \times 3$), horizontal lines are means, and error bars are SD. Statistical significances among multiple cell lines were calculated using one-way ANOVA followed by the Dunnett multiple comparison test.

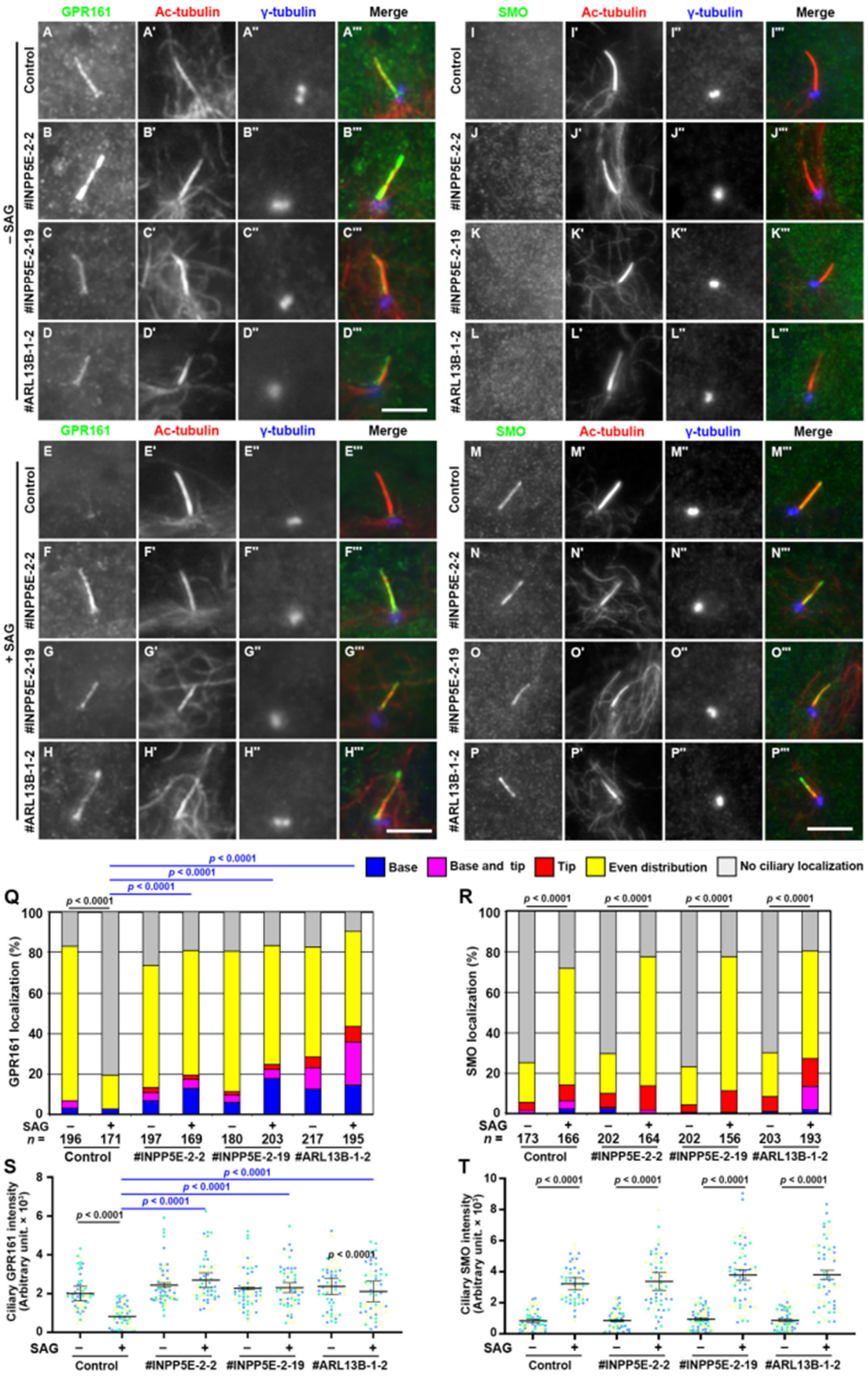
GPR161
Ac-tubulin
γ-tubulin
Merge
SMO
− SAG
+ SAG
Control
#INPP5E-2-2
#INPP5E-2-19
#ARL13B-1-2
Base
Base and tip
Tip
Even distribution
No ciliary localization
p < 0.0001
Q
GPR161 localization (%)
SAG
n =
196 171 197 169 180 203 217 195
Control
#INPP5E-2-2
#INPP5E-2-19
#ARL13B-1-2
R
SMO localization (%)
173 166 202 164 202 156 203 193
S
Ciliary GPR161 intensity (Arbitrary unit. × 10²)
T
Ciliary SMO intensity (Arbitrary unit. × 10²)

Fig. 1-4. Accumulation of GPR161 within cilia in *INPP5E*-KO and *ARL13B*-KO cells
Control RPE1 cells (A, E, I, M), the *INPP5E*-KO cell lines #INPP5E-2-2 (B, F, J, N) and #INPP5E-2-19 (C, G, K, O), and the *ARL13B*-KO cell line #ARL13B-1-2 (D, H, L, P), were serum-starved for 24 h and cultured in the absence (A–D, I–K; –SAG) or presence (E–H, M–P; +SAG) of SAG for a further 24 h, and immunostained with antibodies against either GPR161 (A–H) or SMO (I–P), Ac-tubulin (A′–P′), and γ-tubulin (A″–P″). Scale bars, 5 μm. (Q, R) Localization of GPR161 (Q) and SMO (R) in individual control, *INPP5E*-KO, and *ARL13B*-KO cells was classified as 'localization to ciliary base', 'localization to ciliary base and tip', 'even distribution throughout cilia', 'localization to ciliary tip', and no ciliary localization', and the number of cells in each category was counted. The percentages of these populations are expressed as stacked bar graphs. Values are means of three independent experiments, and the total numbers of cells analyzed (*n*) are indicated. In each set of experiments, 52 to 76 cells (Q) and 52 to 72 cells (R) were analyzed. Statistical significances among multiple cell lines were calculated for the 'base' and 'no localization' categories using two-way ANOVA followed by the Tukey multiple comparison test, and those between two groups (–SAG and +SAG) were calculated using the Student *t*-test. (S, T) Relative ciliary staining intensities of GPR161 (S) and SMO (T) in control, *INPP5E*-KO, and *ARL13B*-KO cells were estimated and expressed as scatter plots. Different colored dots represent three independent experiments ($n = 20 \times 3$), horizontal lines are means, and error bars are SD. Statistical significances among multiple cell lines were calculated using one-way ANOVA followed by the Dunnett multiple comparison test, and those between two groups (–SAG and +SAG) were calculated using the Student *t*-test.

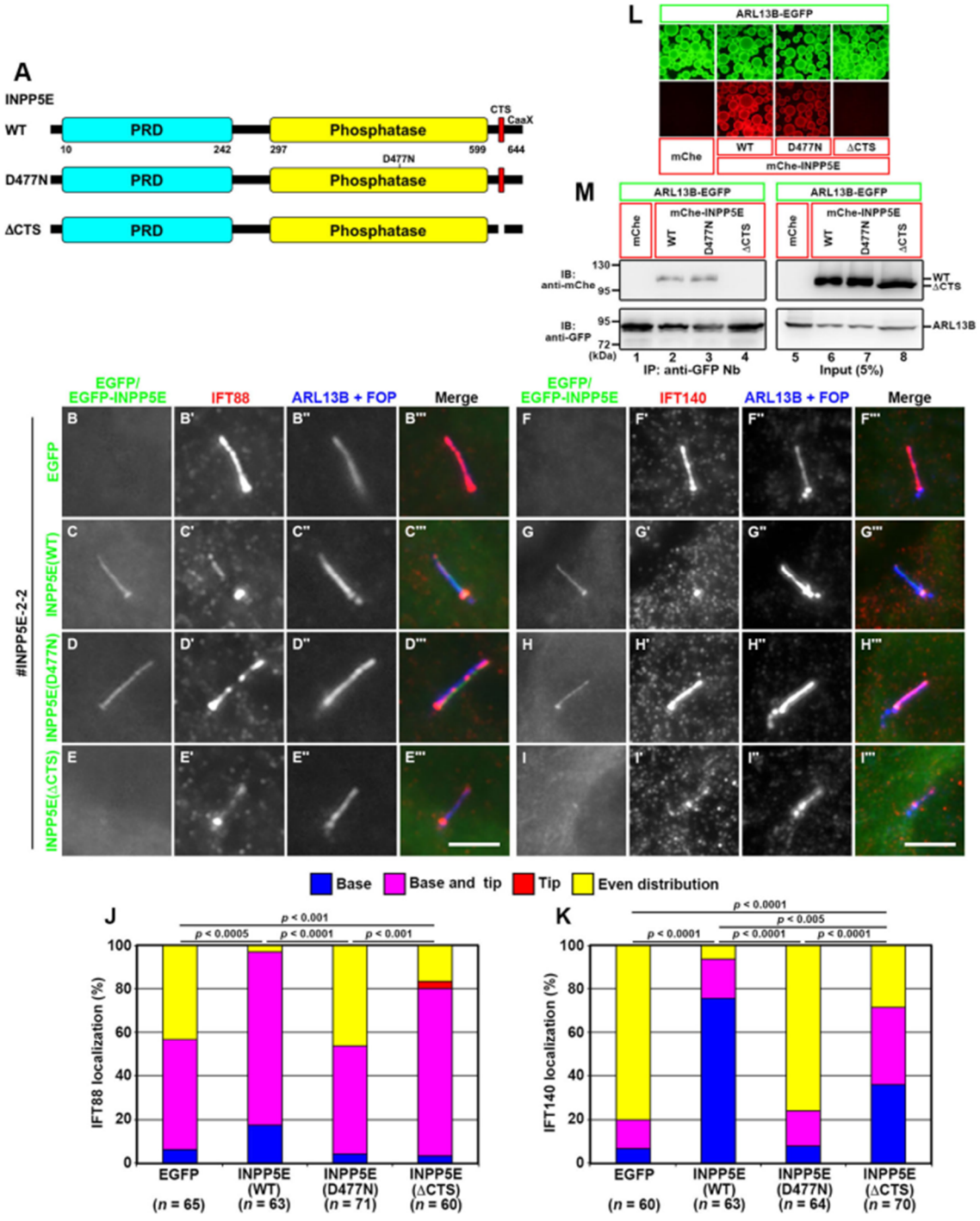
A
INPP5E
WT
PRD
Phosphatase
CTS
CaaX
10
242
297
599
644
D477N
ΔCTS
L
ARL13B-EGFP
mChe
WT
D477N
ΔCTS
mChe-INPP5E
M
IB: anti-mChe
IB: anti-GFP
130
95
72
(kDa)
WT
ΔCTS
ARL13B
IP: anti-GFP Nb
Input (5%)
EGFP/ EGFP-INPP5E
IFT88
ARL13B + FOP
Merge
IFT140
#INPP5E-2-2
EGFP
INPP5E(WT)
INPP5E(D477N)
INPP5E(ΔCTS)
Base
Base and tip
Tip
Even distribution
J
IFT88 localization (%)
p < 0.001
p < 0.0005
p < 0.0001
EGFP (n = 65)
INPP5E (WT) (n = 63)
INPP5E (D477N) (n = 71)
INPP5E (ΔCTS) (n = 60)
K
IFT140 localization (%)
p < 0.0001
p < 0.005
EGFP (n = 60)
INPP5E (WT) (n = 63)
INPP5E (D477N) (n = 64)
INPP5E (ΔCTS) (n = 70)

Fig. 1-5. Rescue of IFT88 and IFT140 localization in *INPP5E*-KO cells upon the stable expression of INPP5E constructs

(A) Schematic representation of the domain organization of INPP5E and its mutants used in this study. PRD, proline-rich domain. (B–I) The *INPP5E*-KO cell line (#INPP5E-2-2) stably expressing EGFP (B, F), EGFP-fused INPP5E(WT) (C, G), INPP5E(D477N) (D, H), or INPP5E(ΔCTS) (E, I) were serum-starved for 24 h, and immunostained for either IFT88 (B′–E′) or IFT140 (F′–I′) and ARL13B + FOP (B″–I″). Scale bars, 5 μm. (J, K) Localization of IFT88 and IFT140 was analyzed as described in the legend for Fig. 1-3, M, N. In each set of experiments, 18 to 25 cells (J) and 18 to 26 cells (K) were analyzed. Statistical significances were calculated for the 'even distribution' category using two-way ANOVA followed by the Tukey multiple comparison test. (L, M). Lysates prepared from HEK293T cells coexpressing ARL13B-EGFP and mChe, mChe-INPP5E(WT), mChe-INPP5E(D477N), or mChe-INPP5E(ΔCTS) were subjected to the VIP assay using anti-GFP Nb (L), followed by immunoblotting analysis using anti-mChe and anti-GFP antibodies (M). IP, immunoprecipitation; IB immunoblotting

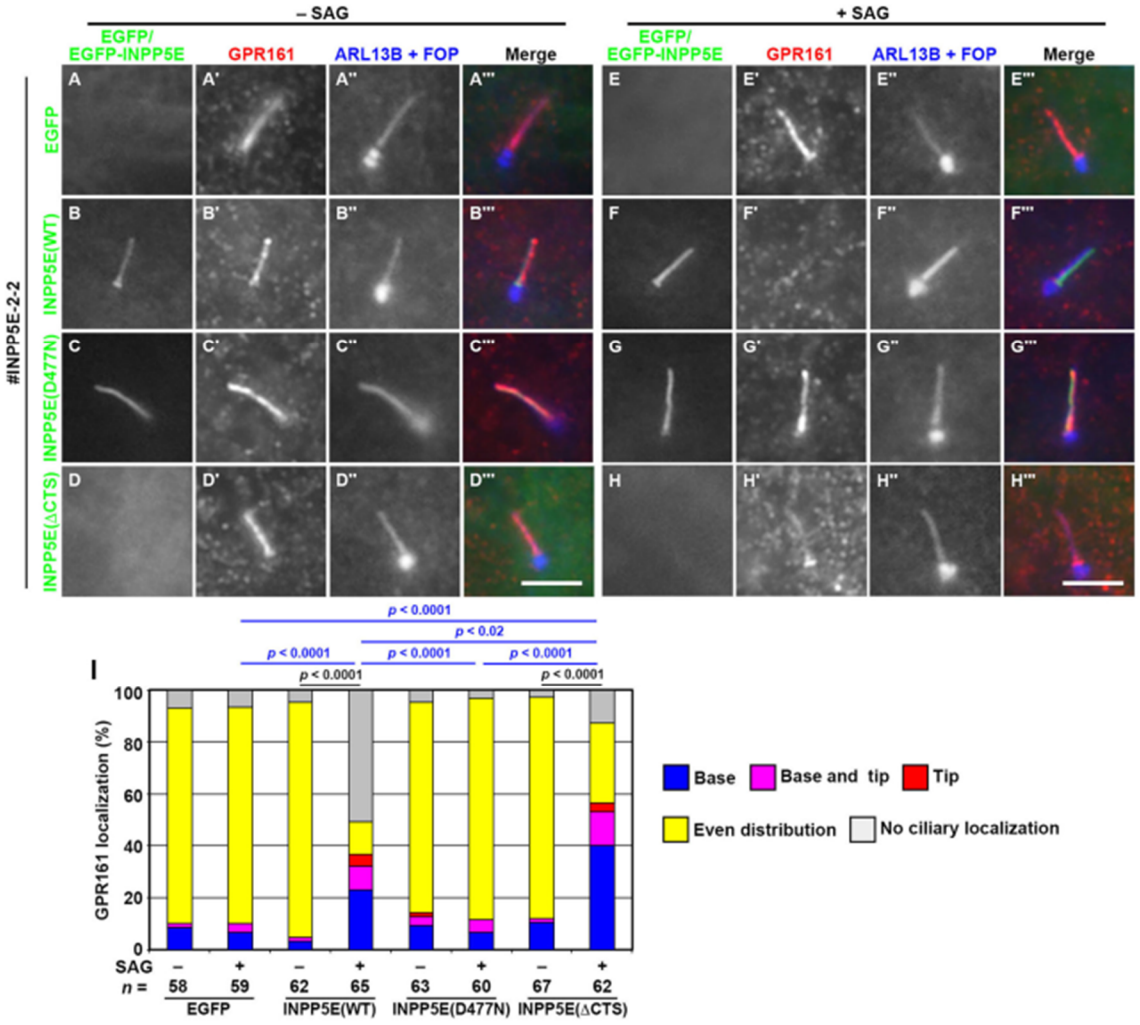

Fig. 1-6. Rescue of GPR161 localization in *INPP5E*-KO cells upon the stable expression of INPP5E constructs

The *INPP5E*-KO cell line #INPP5E-2-2 stably expressing EGFP (A, E), EGFP-fused INPP5E(WT) (B, F), INPP5E(D477N) (C, G), or INPP5E(ΔCTS) (D, H) were treated as described in the legend for Fig. 1-4, and immunostained for GPR161 (A′–H′) and ARL13B + FOP (A″–H″). Scale bars, 5 μm. (I) Localization of GPR161 was analyzed as described in the legend for Fig. 1-4Q. In each set of experiments, 18 to 23 cells were analyzed. Statistical significances among multiple cell lines were calculated for the 'base' and 'no localization' categories using two-way ANOVA followed by the Tukey multiple comparison test, and those between two groups (–SAG and +SAG) were calculated using the Student *t*-test.

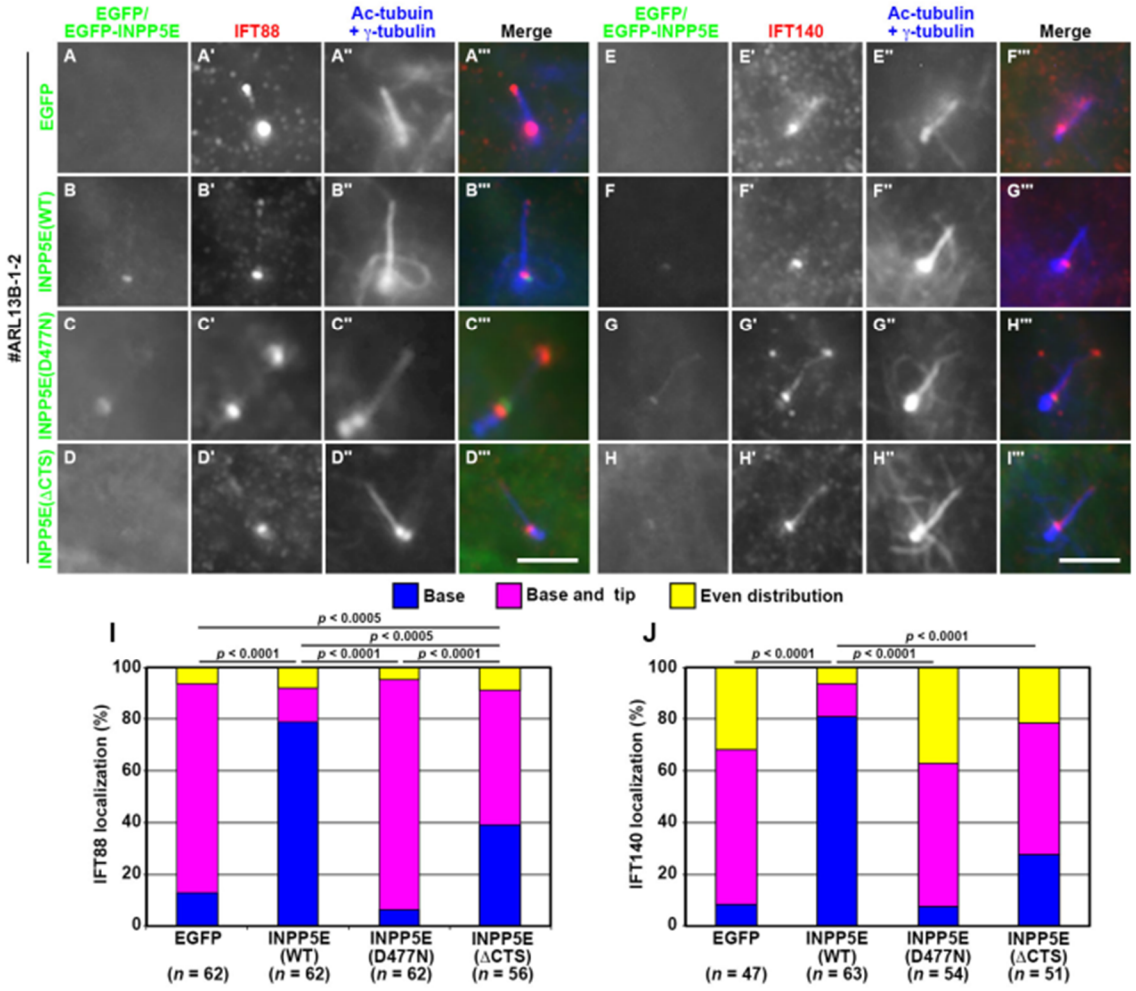

Fig. 1-7. Rescue of IFT88 and IFT140 localization in *ARL13B*-KO cells upon the stable expression of INPP5E constructs

The *ARL13B*-KO cell line (#ARL13B-1-2) expressing EGFP (A, E), EGFP-fused INPP5E(WT) (B, F), INPP5E(D477N) (C, G), or INPP5E(ΔCTS) (D, H) were serum-starved for 24 h, and immunostained for either IFT88 (A′–D′) or IFT140 (E′–H′) and Ac-tubulin + γ-tubulin (A″–H″). Scale bars, 5 μm. (I, J) Localization of IFT88 and IFT140 was analyzed as described in the legend for Fig. 1-3, M, N. In each set of experiments, 18 to 21 cells (I) and 15 to 21 cells (J) were analyzed. Statistical significances were calculated for the 'base and tip' categories using two-way ANOVA followed by the Tukey multiple comparison test.

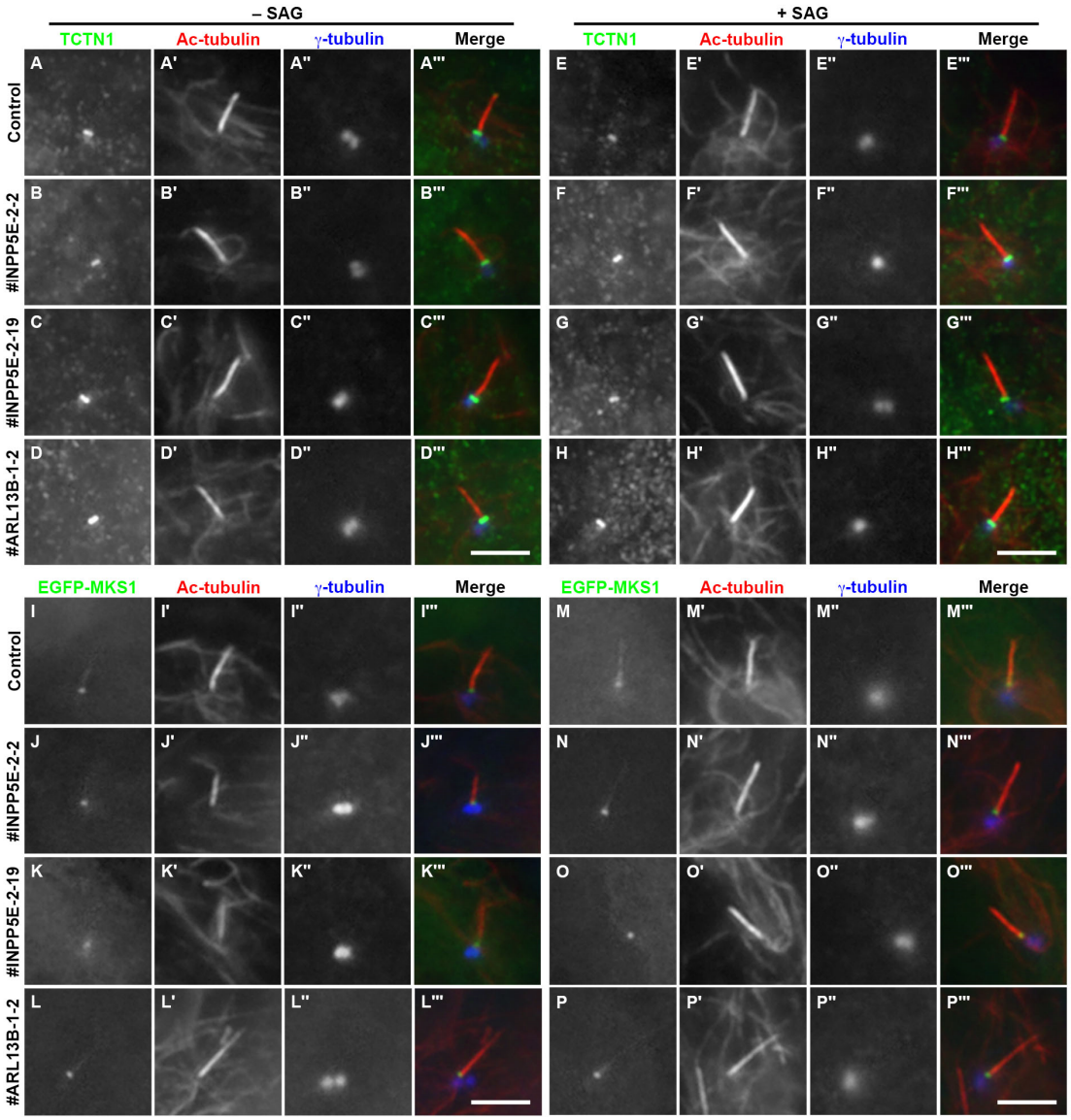

Fig. 1-8. Integrity of the TZ in *INPP5E*-KO and *ARL13B*-KO cells

(A–H) Control RPE1 cells (A, E), the *INPP5E*-KO cell lines #INPP5E-2-2 (B, F) and #INPP5E-2-19 (C, G), and the *ARL13B*-KO cell line #ARL13B-1-2 (D, H) were serum-starved for 24 h, and cultured in the absence (A–D; –SAG) or presence (E–H; +SAG) of 200 nM SAG for a further 24 h, and immunostained with antibodies against TCTN1 (A–H), Ac-tubulin (A′–H′), and γ-tubulin (A″–H″). (I–P) Control RPE1 cells (I, M), the *INPP5E*-KO cell lines #INPP5E-2-2 (J, N) and #INPP5E-2-19 (K, O), and the *ARL13B*-KO cell line #ARL13B-1-2 (L, P) stably expressing EGFP-MKS1 were serum-starved for 24 h, and cultured in the absence (I–K; –SAG) or presence (M–P; +SAG) of 200 nM SAG for a further 24 h. The cells were immunostained with antibodies against Ac-tubulin (I′–P′) and γ-tubulin (I″–P″). Scale bars, 5 μm.

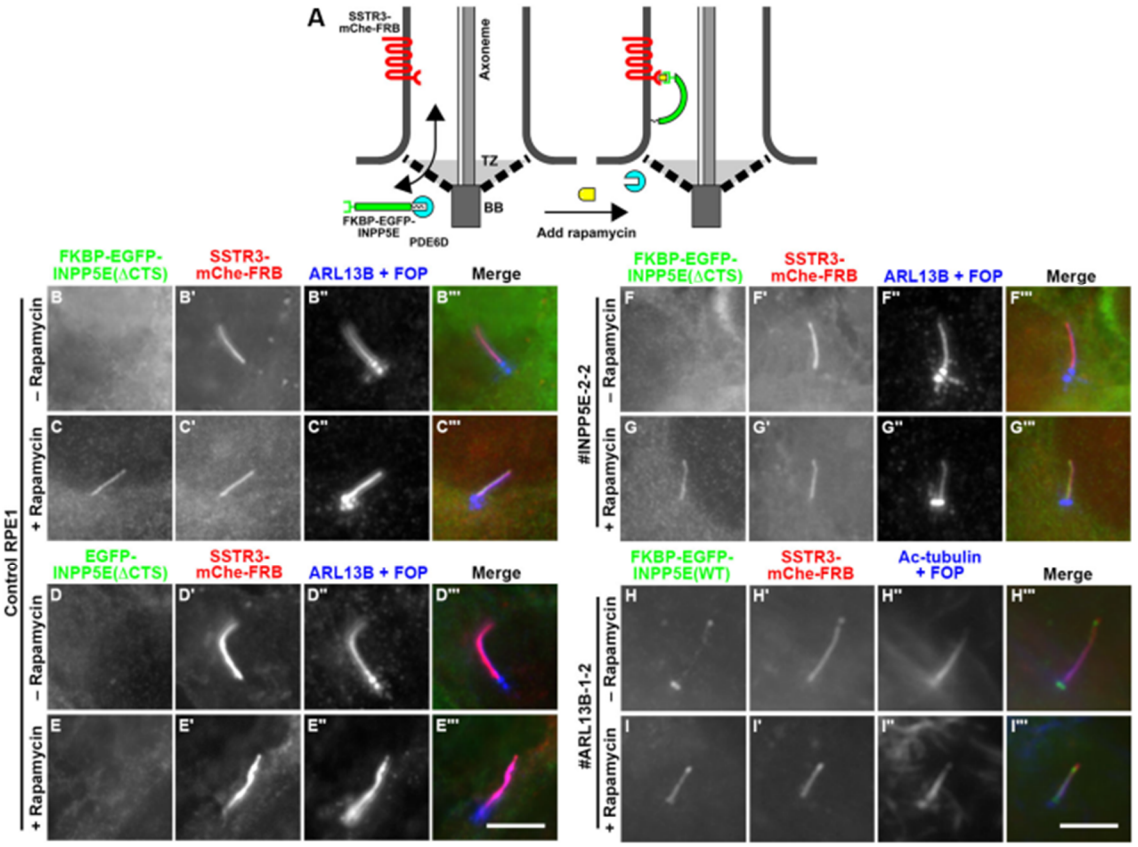

Fig. 1-9. INPP5E–ARL13B interaction is dispensable for INPP5E entry into cilia

(A) Schematic representation of the design of the CID experiment to enable controlled entry of the INPP5E constructs into cilia. In this model, it is assumed that PDE6D dissociates from INPP5E on the cytosolic side of the TZ. (B–G) Control RPE1 (B–E), *INPP5E*-KO (F, G), and *ARL13B*-KO (H, I) cells stably expressing the SSTR3-mChe-FRB construct were infected with a lentiviral vector for FKBP-EGFP-INPP5E(ΔCTS) (B, C, F, G), EGFP-INPP5E(ΔCTS) (D, E) or FKBP-EGFP-INPP5E(WT) (H, I). The cells were left untreated (B, D, F, H) or treated with 200 nM rapamycin for 15 min (C, E, G, I), immunostained with an anti-GFP antibody (B–I) and anti-ARL13B + anti-FOP antibodies (B″–G″) or anti-Ac-tubulin + anti-FOP antibodies (H″, I″), and observed under a microscope. Scale bars, 5 μm.

DISCUSSION

Prior to this study, two possible roles of ARL13B in the targeting of INPP5E to the ciliary membrane were proposed, although they are not mutually exclusive. One is that ARL13B determines the ciliary membrane localization of INPP5E by directly interacting with the CTS (Humbert et al., 2012; Nozaki et al., 2017); and the other is that ARL13B indirectly determines the ciliary localization of INPP5E by acting as a GEF for ARL3, which promotes the release of PDE6D from prenylated INPP5E (Gotthardt et al., 2015; Ivanova et al., 2017; Stephen and Ismail, 2016; Zhang et al., 2016).

The data presented here support the former possibility that the interaction of INPP5E with ARL13B via the CTS is crucial for its retention on the ciliary membrane. Namely, INPP5E(ΔCTS) in control RPE1 cells and INPP5E(WT) in *ARL13B*-KO cells were able to enter cilia but were unable to be retained on the ciliary membrane. In view of the fact that defects in the localization of the components of the IFT machinery and GPR161 were rescued in these cells, the transient entry of exogenously expressed INPP5E molecules into cilia may be sufficient to hydrolyze PtdIns(4,5)P_2 to PtdIns(4)P in the ciliary membrane. These results are compatible with the fact that the phenotypes of *INPP5E*-KO and *ARL13B*-KO cells closely resemble each other (Figs. 1-3 and 1-4). In this context, it is important to note the recent study of Gigante et al. showing that knock-in mice of Arl13b(V358A), which is an Arl13b variant defective in ciliary localization due to a Val-to-Ala substitution in the VxP ciliary targeting motif (Higginbotham et al., 2012), showed apparently normal Hh signaling, even though ciliary localization of INPP5E was not observed (Gigante et al., 2020). Thus, similarly to INPP5E(ΔCTS), the cilia-excluded Arl13b(V358A) variant might be able to enter cilia but unable to be retained on the ciliary membrane, although it is unknown as to how the VxP motif participates in the ciliary targeting of ARL13B. However, it is also possible that INPP5E(ΔCTS) in control cells and INPP5E(WT) in *ARL13B*-KO cells could function from outside cilia, rather than transient entry into cilia. For example, INPP5E could indirectly affect ciliary protein trafficking through modifying lipid composition on the plasma membrane or on vesicles required for cilia biogenesis.

However, my data does not rule out the latter possibility, which is associated with the important question of where prenylated INPP5E is released from PDE6D, as INPP5E(ΔCTS) retains the ability to undergo prenylation and thereby to be captured by PDE6D in the cytosol. Previous studies showed that INPP5E constructs lacking the C-terminal CaaX motif for prenylation were able to localize to cilia in a PDE6D-independent manner, although their ciliary levels were lower than that of INPP5E(WT)

(Humbert et al., 2012; Kösling et al., 2018; Thomas et al., 2014). Thus, without the C-terminal prenylation, INPP5E appears to be able to undergo passage across the ciliary gate, even though the efficiency is low. Once entering cilia, INPP5E molecules without prenylation are likely to be trapped by ARL13B. However, in PDE6D-depleted and *PDE6D*-KO cells, INPP5E or another prenylated protein, RPGR, was not detectable within cilia (Dutta and Seo, 2016; Thomas et al., 2014; Zhang et al., 2019), indicating that for proteins with C-terminal prenylation, PDE6D is crucial for their solubilization in the cytosol (Fansa et al., 2016). As INPP5E constructs without a prenylation site are expected to act as soluble proteins, the soluble and prenylated proteins are likely to use distinct mechanisms to pass the ciliary gate.

If INPP5E enters cilia across the ciliary gate as a complex with PDE6D, the INPP5E–PDE6D complex must permeate the gate by acting as a soluble protein of approximately 85 kDa (~70 kDa + ~15 kDa). On the other hand, if INPP5E is released from PDE6D and anchored to the lipid bilayer via its prenyl moiety before crossing the ciliary gate, INPP5E is expected to pass the gate by lateral diffusion. Previous studies suggested that the ciliary gate acts as a size-exclusion permeability barrier for soluble proteins; the entry rate decreases as protein size increases, with entry not detectable for proteins greater than 100 kDa (Breslow et al., 2013; Kee et al., 2012; Takao and Verhey, 2016). Another kinetic study using the CID system showed that larger proteins have the potential to enter cilia through the molecular sieve, albeit with reduced kinetics (Lin et al., 2013). On the other hand, the ciliary entry of specific transmembrane proteins, including class A GPCRs and polycystins, across the ciliary gate is known to be mediated by the TULP3 adaptor protein together with the IFT-A complex (Badgandi et al., 2017; Hirano et al., 2017; Kobayashi et al., 2021; Mukhopadhyay et al., 2010; Park et al., 2013). It is likely that TULP3 captures the ciliary localization sequences of these transmembrane proteins in a PtdIns(4,5)P_2-dependent manner on the plasma membrane side of the ciliary gate, and releases them on the ciliary membrane side, where the PtdIns(4,5)P_2 level is low owing to the presence of INPP5E (Badgandi et al., 2017).

However, relatively little is known about how lipidated membrane proteins cross the ciliary gate (Jensen and Leroux, 2017). In other words, although lipidated membrane proteins are first trapped by the solubilizing factor PDE6D or UNC119 in the cytosol, it is presently unclear whether these proteins are released from the solubilizing factor with the aid of ARL3 on the plasma membrane or the ciliary membrane side of the gate. If ARL3 is active on the cytosolic side, INPP5E can be released and anchored to the plasma membrane to cross the ciliary gate by lateral diffusion. If ARL3 requires ARL13B for its activation, the INPP5E–PDE6D complex must permeate the ciliary gate in some way, to

retrieve PDE6D from INPP5E by activated ARL3 within cilia, and then INPP5E is anchored to the ciliary membrane, where it is retained via its binding to ARL13B. In this context, although attempts of our research group to show the steady-state localization of endogenous or exogenously expressed ARL3 has not been successful to date, ARL3 is expected to readily permeate the molecular sieve of the ciliary gate, considering its small size (Kee et al., 2012; Kösling et al., 2018; Lin et al., 2013).

In conclusion, the present study demonstrates that binding of INPP5E to ARL13B is essential for its retention on the ciliary membrane, but is not necessary for its entry into cilia.

Chapter 2: The molecular basis of ciliary defects caused by combinations of deletion and missense variants of dynein-2 DYNC2LI1 subunit found in skeletal ciliopathies

ABSTRACT

Cilia play crucial roles in sensing and transducing extracellular signals. Bidirectional protein trafficking within cilia is mediated by the intraflagellar transport (IFT) machinery containing IFT-A and IFT-B complexes, with the aid of kinesin-2 and dynein-2 motors. The dynein-2 complex drives retrograde trafficking of the IFT machinery after its transportation to the ciliary tip as an IFT cargo. Mutations in genes encoding the dynein-2-specific subunits (DYNC2H1, WDR60, WDR34, DYNC2LI1, and TCTEX1D2) are known to cause skeletal ciliopathies. I here demonstrate that several pathogenic variants of DYNC2LI1 are compromised regarding their ability to interact with DYNC2H1 and WDR60. When expressed in DYNC2LI1-knockout cells, deletion variants of DYNC2LI1 were unable to rescue the ciliary defects of these cells, whereas missense variants, as well as wild-type DYNC2LI1, restored the normal phenotype. DYNC2LI1-knockout cells coexpressing one pathogenic deletion variant together with wild-type DYNC2LI1 demonstrated a normal phenotype. In striking contrast, DYNC2LI1-knockout cells coexpressing the deletion variant in combination with a missense variant, which mimics the situation of cells of compound heterozygous ciliopathy individuals, demonstrated ciliary defects. Thus, DYNC2LI1 deletion variants found in individuals with skeletal ciliopathies cause ciliary defects when combined with a missense variant, which expressed on its own does not cause substantial defects.

INTRODUCTION

The movement of cargos (proteins, and membrane-bound vesicles and organelles) along microtubules, as well as the remodeling of microtubules during cell division, are coordinately controlled by motor proteins. In general, the kinesin and dynein motors drive plus- and minus-end directed movements of cargos, respectively (Hirokawa et al., 2010).

Cilia are microtubule-based projections from the surfaces of a variety of eukaryotic cells, and perceive and transduce mechanical signals. Owing to the crucial roles of cilia in development and homeostasis of organisms, their dysfunction causes a heterogenous group of disorders known as the ciliopathies, which demonstrate a broad spectrum of symptoms, including skeletal and brain malformation (Mitchison and Valente, 2017; Reiter and Leroux, 2017).

Not only bidirectional protein trafficking within cilia, but also the entry and exit of proteins across the ciliary gate composed of the TZ is mediated by the IFT machinery (Prevo et al., 2017; Nakayama and Katoh, 2018). Within the IFT machinery, the IFT-B complex, which is composed of 16 subunits, mediates anterograde trafficking driven by the kinesin-II motor, and the export of ciliary membrane proteins across the TZ together with the BBSome. On the other hand, the IFT-A complex, which is composed of six subunits, mediates retrograde trafficking driven by dynein-2 (also known as IFT dynein) and the import of ciliary GPCRs across the TZ together with the TULP3 adaptor (Mukhopadhyay et al., 2017; Nachury and Mick, 2019; Nakayama and Katoh, 2020). In addition, recent studies in *Caenorhabditis elegans* suggested that the IFT-A complex and IFT dynein are required for the integrity and gating function of the TZ (Jensen et al., 2018; Scheidel and Blacque, 2018).

Dynein-2/IFT dynein is a very large protein complex that is composed of five subunits specific to dynein-2 (the DYNC2H1 heavy chain, the WDR60 and WDR34 intermediate chains [recently renamed as DYNC2I1 and DYNC2I2, respectively], the DYNC2LI1 light intermediate chain [LIC], and the TCTEX1D2 light chain [recently renamed as DYNLT2B]), and three-types of light chains shared with the dynein-1 complex (DYNLL1/DYNLL2, DYNLRB1/DYNLRB2, and DYNLT1/DYNLT3) (Nakayama and Katoh, 2020; Vuolo et al., 2020; Webb et al., 2020) (see Fig. 2-1). Biochemical and interactome analyses by our research group and others delineated the architectural model of the mammalian dynein-2 complex (Asante et al., 2014; Hamada et al., 2018; Vuolo et al., 2018; Tsurumi et al., 2019), in which DYNC2LI1 forms a subcomplex with the N-terminal tail (nonmotor) region of DYNC2H1, which in turn interacts with WDR60 and WDR34. The model proposed by our research group is largely

consistent with the recently clarified cryo-EM structure of the human dynein-2 complex (Toropova et al., 2019), in which two molecules of DYNC2H1 adopt asymmetric conformations in the tail region, with each DYNC2H1 molecule binding to DYNC2LI1, and either WDR60 or WDR34. Docking of the dynein-2 structure into the anterograde IFT train structure of *Chlamydomonas* flagella (Jordan et al., 2018) clarified by cryoelectron tomography suggested that each dynein-2 complex spans out multiple IFT-B repeats when it is transported as a cargo of the anterograde IFT train (Toropova et al., 2019). In agreement with the docking model, interactome analyses of WDR60 and WDR34 suggested that dynein-2 interacts with multiple IFT-B subunits (Vuolo et al., 2018). Furthermore, it is interesting to note that while this study was in progress, the DYNC2LI1 ortholog in *Chlamydomonas* was reported to interact with the IFT-B subunit IFT54, and the DYNC2LI1–IFT54 interaction was suggested to be crucial for the transport of dynein-2 as a cargo of the anterograde IFT train (Zhu et al., 2021).

In line with the cooperative role of the IFT-A and dynein-2 complexes in retrograde trafficking, mutations of all IFT-A subunits and dynein-2-specific subunits are known to cause skeletal ciliopathies characterized by a narrow thorax and polydactyly, generally termed short-rib thoracic dysplasia (SRTD), including short rib-polydactyly syndrome (SRPS), Jeune asphyxiating thoracic dystrophy (JATD), Ellis-van Creveld syndrome (EvC), and cranioectodermal dysplasia (CED) (Lin et al., 2013; Arts and Knoers, 2013 [updated 2018]; Schmidts, 2014; Corés et al., 2015; McInerney-Leo et al., 2015; Reiter and Leroux, 2017; Zhang et al., 2018). Our research group recently demonstrated the molecular basis of the ciliary defects caused by CED-associated variations of the IFT-A subunits IFT122 and IFT144/WDR19 (Takahara et al., 2018; Ishida et al., 2021). In this study, I focused on DYNC2LI1, which is the causative gene of SRPS/SRTD15, as several pathogenic biallelic variations were reported (Kessler et al., 2015; Taylor et al., 2015; Niceta et al., 2018; Zhang et al., 2020). I here show that several DYNC2LI1 variants have reduced abilities to bind DYNC2H1 and WDR60. More importantly, I found that in *DYNC2LI1*-KO cells, the expression of a single deletion variant in combination with a missense variant causes substantial ciliary defects, but not in combination with wild-type (WT) DYNC2LI1.

RESULTS

Variations of DYNC2LI1 found in SRTD individuals affect its interactions with DYNC2H1 and WDR60

As DYNC2LI1 interacts directly with the DYNC2H1 heavy chain (Hamada et al., 2018; Toropova et al., 2019), I first determined which region(s) of the DYNC2LI1 protein participates in its interaction with DYNC2H1. The previously revealed X-ray crystallographic structure of the dynein-1 LIC of thermophilic yeast and biochemical experiments of our research group using human DYNC1LI1 demonstrated that DYNC1LI1 interacts with DYNC1H1 via the N-terminal Ras-like G domain (see Fig. 2-2A), which is evolutionally conserved among the LICs of the dynein-1 and dynein-2 complexes (Schroeder et al., 2014). In addition, the cryo-EM structure of the dynein-2 complex indicated that both the G domain and the C-terminal coil region of DYNC2LI1 participate in its interaction with DYNC2H1 (Toropova et al., 2019). In addition, there is a relatively long α-helical coil region (residues 318–352) at the C-terminus of DYNC2LI1 (see Fig. 2-2A) (Kessler et al., 2015). I therefore made some DYNC1LI1 constructs with truncations from the C-terminus, and analyzed their interactions with the N-terminal tail region (residues 1–1,090) of DYNC2H1 [hereafter referred to as DYNC2H1(N)]. Lysates prepared from HEK293T cells coexpressing DYNC2H1(N)-mCherry (mChe) and any of the DYNC2LI1 constructs fused to EGFP were subjected to immunoprecipitation with glutathione S-transferase (GST)-fused anti-mChe nanobodies (Nb) (LaM-2 version) (Ishida et al., 2021) prebound to glutathione-Sepharose beads, followed by SDS-PAGE and immunoblotting analysis using anti-mChe and anti-GFP antibodies. As shown in Fig. 2-2C, EGFP-DYNC2LI1(WT) was coimmunoprecipitated with DYNC2H1(N)-mChe but not with mChe alone (compare lanes 1 and 2). The DYNC2LI1(1–317) construct, which lacks the C-terminal coil region (see Fig. 2-2A), was much less efficiently coprecipitated with DYNC2H1(N)-mChe than DYNC2LI1(WT) (Fig. 2-2C, compare lanes 2 and 9). The amounts of the other truncation constructs, DYNC2LI1(1–297) and DYNC2LI1(1–240), coprecipitated with DYNC2H1(N)-mChe were also substantially lower than that of DYNC2LI1(WT) (compare lanes 8 and 10 with lane 2). On the other hand, the C-terminal construct DYNC2LI1(241–352) was not coprecipitated with DYNC2H1(N)-mChe (lane 11). These results are consistent with the dynein-2 cryo-EM structure, which indicates the contribution of the C-terminal coil region as well as the G domain of DYNC2LI1 to its interaction with DYNC2H1 (Toropova et al., 2019).

To date, four studies have identified compound heterozygous variations in DYNC2LI1 in individuals showing phenotypes of the skeletal ciliopathies (see Table 2-1) (Kessler et al., 2015; Taylor et al., 2015; Niceta et al., 2018; Zhang et al., 2020). One case study reported combinations of a missense variant DYNC2LI1(L117V) with the deletion/truncation variant DYNC2LI1(Δ302–332) or DYNC2LI1(W124*) (Taylor et al., 2015) in individuals showing phenotypes of the skeletal ciliopathies. In two other case studies, affected individuals were found to have combinations of the missense variant DYNC2LI1(T221I), and the truncation variant DYNC2LI1(R208*) [hereafter referred to as DYNC2LI1(1–207)], DYNC2LI1(V141*), or DYNC2LI1, which has a mutation at the initiation codon (Kessler et al., 2015; Niceta et al., 2018). While this study was underway, a study reported a combination of the missense variant DYNC2LI1(P120S) and a truncation variant DYNC2LI1(K310*) in an affected individual (Zhang et al., 2020). Among the deletion/truncation variants, I selected DYNC2LI1(Δ302–332) and DYNC2LI1(1–207), and analyzed their interactions with DYNC2H1. I was also interested in three missense variants, DYNC2LI1(L117V), DYNC2LI1(P120S), and DYNC2LI1(T221I), as these mutated residues are conserved not only in DYNC2LI1 but also in the dynein-1 LICs, DYNC1LI1 and DYNC1LI2 (see Fig. 2-2B).

As expected from the analysis of the C-terminal truncation variants described above, DYNC2LI1(Δ302–332) and DYNC2LI1(1–207) were found to have substantially reduced abilities to interact with DYNC2H1, compared with DYNC2LI1(WT) (Fig. 2-2C, compare lanes 3 and 5 with lane 2). Among the missense variants, DYNC2LI1(T221I) retained DYNC2H1-binding ability to a level comparable to that of DYNC2LI1(WT) (lane 7), whereas DYNC2LI1(L117V) and DYNC2LI1(P120S) had reduced DYNC2H1-binding ability (lanes 4 and 6). It is of note that the amount of the DYNC2H1(N)-mChe protein tends to be reduced when coexpressed with any of the DYNC2LI1 constructs with reduced interacting abilities (Fig. 2-2C, input panel); therefore, DYNC2H1(N) might be unstable in the absence of its efficient interaction with DYNC2LI1 (also see below).

As a previous study of our research group indicated that a subcomplex of DYNC2H1 and DYNC2LI1 efficiently interacts with the C-terminal WD40 repeat region of WDR60/DYNC2I1 (Hamada et al., 2018), I then analyzed the interactions of WDR60(627–1,066) with a combination of DYNC2H1(N) and any of the DYNC2LI1 constructs. The results shown in Fig. 2-2D correlated well with those for the binary interactions between DYNC2H1(N) and the DYNC2LI1 construct shown in Fig. 2-2C; namely, mChe-WDR60(627–1,066) was coimmunoprecipitated with DYNC2H1(N)-EGFP when combined with EGFP-DYNC2LI1(T221I) as efficiently as when combined with EGFP-DYNC2LI1(WT) (Fig. 2-2D, lanes 2 and 7); in striking contrast,

coprecipitation of mChe-WDR60(627–1,066) was abolished when DYNC2H1(N)-EGFP was combined with any other DYNC2LI1 construct (lanes 3–6 and lanes 8–11). Thus, it is likely that WDR60 interacts efficiently with the DYNC2H1–DYNC2LI1 dimer but not with DYNC2H1 alone. Again, it is of note that DYNC2H1(N) appeared to be unstable in the absence of its efficient interaction with DYNC2LI1 (Fig. 2-2D, input panel), although we did not pursue this issue further.

Previous studies of our research group also suggested that although DYNC2H1 alone can interact with the WD40 repeat region of WDR34, its efficient interaction with WDR34 requires its subcomplex formation with DYNC2LI1 (Hamada et al., 2018; Tsurumi et al., 2019). I therefore analyzed the interactions of WDR34(106–536) with a combination of DYNC2H1(N) and any of the DYNC2LI1 constructs. However, in contrast to the results obtained for WDR60 (Fig. 2-2D), the amount of mChe-WDR34(106–536) coimmunoprecipitated with DYNC2H1(N)-EGFP did not substantially vary in the presence of any of the coexpressed EGFP-DYNC2LI1 constructs (Fig. 2-3A). Thus, it is likely that WDR34 interacts primarily with DYNC2H1, and that the DYNC2LI1 variations found in SRTD do not considerably affect the interaction of WDR34 with DYNC2H1–DYNC2LI1.

While this study was in progress, a study using Chlamydomonas reported that IFT54, which is a subunit of the IFT-B complex, binds to IFT dynein via the DYNC2LI1 ortholog, and suggested that the IFT54–DYNC2LI1 interaction is crucial for anterograde trafficking of the dynein-2 complex, as a cargo of the IFT machinery (Zhu et al., 2021). I therefore analyzed the interactions of human IFT54 with the various DYNC2LI1 constructs. As shown in Fig. 2-3B, I confirmed that mChe-IFT54 coimmunoprecipitated with EGFP-DYNC2LI(WT) (lane 2). Regarding the DYNC2LI1 variants, DYNC2LI1(241–352) (lane 11) lacked the ability to interact with IFT54, and DYNC2LI1(1–207) and DYNC2(1–240) (lanes 5 and 10) appeared to have substantially reduced IFT54-binding ability. These results indicate that DYNC2LI1 interacts with IFT54 mainly via the G domain, and that the missense variations of DYNC2LI1 found in SRTD do not substantially affect its interaction with IFT54.

Defects of ciliary protein trafficking in *DYNC2LI1*-KO cells exogenously expressing DYNC2LI1 variants

To analyze the functional defects of the DYNC2LI1 variants, I first established *DYNC2LI1*-KO cells from human telomerase reverse transcriptase-immortalized retinal pigment epithelial 1 (hTERT-RPE1) cells using the CRISPR/Cas9 system (Katoh et al., 2017). The *DYNC2LI1*-KO cell line #DYNC2LI1-3-2 (Fig. 2-4, A, B) was found to have

very short cilia, when stained with antibodies against ARL13B (a marker of the ciliary membrane), acetylated α-tubulin (Ac-tubulin; a marker of the ciliary axoneme), and γ-tubulin (a marker of the basal body) (see Fig. 2-4, C, D; also see Fig. 2-5Aa). The ciliogenesis defect observed in the #DYNC2LI1-3-2 cell line did not result from off-target effects of the CRISPR/Cas9 system, as the exogenous expression of mChe-DYNC2LI1(WT), but not mChe alone, restored normal ciliary length (compare Fig. 2-5, A and B; also see Fig. 2-5K).

As for the C-terminal truncation variants, the exogenous expression of mChe-DYNC2LI1(1–317) in *DYNC2LI1*-KO cells partially restored ciliogenesis (Fig. 2-5C), whereas the expression of mChe-fused DYNC2LI1(1–297) or DYNC2LI1(1–240) did not (Fig. 2-5, D, E; also see Fig. 2-5K). In addition, IFT88 appeared to be enriched within very short cilia (see below).

I then analyzed whether the DYNC2LI1 variants found in SRTD individuals are able to rescue the ciliogenesis defect of *DYNC2LI1*-KO cells. The expression of mChe-DYNC2LI1(Δ302–332) partially rescued the ciliogenesis defect (Fig. 2-5F), as for the expression of mChe-DYNC2LI1(1–317) (Fig. 2-5C; also see Fig. 2-5K). Somewhat unexpected was the phenotype of *DYNC2LI1*-KO cells expressing mChe-DYNC2LI1(1–207) (Fig. 2-5G); these cells had cilia that were significantly longer than those expressing DYNC2LI1(WT) (Fig. 2-5K) (see Discussion). I also analyzed the effects of the expression of missense SRTD variants in *DYNC2LI1*-KO cells, and found that all the variants, namely, DYNC2LI1(L117V), DYNC2LI1(P120S), and DYNC2LI1(T221I) had normal ciliary lengths (Fig. 2-5, H–J; also see Fig. 2-5K).

I also analyzed the localization of IFT88 (an IFT-B subunit) in *DYNC2LI1*-KO cells expressing DYNC2LI1 variants, as previous studies of our research group showed that KO cells of other dynein-2 subunits demonstrated significant accumulation of IFT machinery components within cilia. This was also the case for *DYNC2LI1*-KO cells; *DYNC2LI1*-KO cells expressing mChe alone demonstrated the enrichment of IFT88 within short cilia, whereas this enrichment was eliminated by the expression of mChe-DYNC2LI1(WT) (compare Fig. 2-5, A and B; also see Fig. 2-5L). Ciliary IFT88 enrichment was not eliminated by the expression of DYNC2LI C-terminal truncation variants, i.e., DYNC2LI1(1–317), DYNC2LI1(1–297), or DYNC2LI1(1–240), or by the expression of DYNC2LI1(Δ302–332) (Fig. 2-5, C–F; also see Fig. 2-5L). By contrast, the missense variants restored the normal IFT88 localization at the ciliary base (Fig. 2-5, H–J), comparable to DYNC2LI1(WT) (see Fig. 2-5L). In *DYNC2LI1*-KO cells expressing DYNC2LI1(1–207), the enrichment of IFT88 in cilia was partially reduced (Fig. 2-5G; also see Fig. 2-5L).

I then analyzed the localization of GPR161 in *DYNC2LI1*-KO cells expressing the DYNC2LI1 variants; GPR161 is localized on the ciliary membrane under basal conditions to suppress Hh signaling, and it exits cilia upon Hh pathway stimulation (Kopinke et al., 2021). In *DYNC2LI1*-KO cells expressing mChe-DYNC2LI1(WT), GPR161 was found within cilia under basal conditions and became undetectable when the cells were treated with Smoothened agonist (SAG) (Fig. 2-6, B, L). By contrast, in *DYNC2LI1*-KO cells expressing mChe alone, GPR161 was retained within short cilia even in the presence of SAG (Fig. 2-6, A, K), indicating that exit of GPR161 from cilia is suppressed in *DYNC2LI1*-KO cells. Essentially the same results were obtained for *DYNC2LI1*-KO cells expressing DYNC2LI1(1–317), DYNC2LI1(1–297), DYNC2LI1(1–240), or DYNC2LI1(Δ302–332); namely, GPR161 was significantly retained within short cilia even when the cells were treated with SAG (Fig. 2-6, C–F and M–P; also see Fig. 2-6U). In *DYNC2LI1*-KO cells expressing DYNC2LI1(1–207), the basal ciliary level of GRP161 was relatively low, but the level was not significantly decreased even upon SAG treatment (Fig. 2-6, G, Q; also see Fig. 2-6U). By contrast, in *DYNC2LI1*-KO cells expressing any of the missense variants, the ciliary GRP161 level was significantly decreased when the cells were treated with SAG (Fig. 2-6, H–J, and R–T; also see Fig. 2-6U), as in DYNC2LI1(WT)-expressing cells (Fig. 2-6, B, L).

Specific combinations of DYNC2LI1 variants are unable to rescue the ciliary defects in *DYNC2LI1*-KO cells

As described above, all the reported individuals with skeletal ciliopathies caused by variations in DYNC2LI1 have compound heterozygous mutations (Table 2-1). Therefore, I then addressed how combinations of the DYNC2LI1 variants contribute to the ciliary defects. To this end, I expressed the DYNC2LI1 variants in *DYNC2LI1*-KO cells in the combinations found in compound heterozygous individuals, and analyzed the phenotypes of these cells.

I first analyzed the effects of expression of the combination of DYNC2LI1(L117V) and DYNC2LI1(Δ302–332) in *DYNC2LI1*-KO cells, which mimics the cellular situation of an SRPS individual reported by Taylor et al. (Taylor et al., 2015). It is noteworthy that the same study reported the DYNC2LI1(L117V) variation [in combination with DYNC2LI1(W124*)] in one other SRPS individual and the DYNC2LI1(Δ302–332) variation [in combination with DYNC2LI1(E335*)] in another individual (Taylor et al., 2015). As described above (Fig. 2-5), *DYNC2LI1*-KO cells expressing mChe-DYNC2LI1(Δ302–332) showed defects in ciliogenesis and ciliary IFT88 level (Fig. 2-7A), whereas those expressing mChe-DYNC2LI1(L117V) did not show either defect (Fig.

2-7D). When mChe-fused DYNC2LI1(Δ302–332) and DYNC2LI1(WT) were coexpressed in *DYNC2LI1*-KO cells, a situation that mimics cells of a healthy parent of an affected individual, both normal ciliary length and low ciliary IFT88 level were significantly restored (Fig. 2-7B; also see Fig. 2-7, M, N). In striking contrast, when DYNC2LI1(Δ302–332) was coexpressed together with DYNC2LI1(L117V), ciliogenesis was not significantly recovered and ciliary IFT88 enrichment was not significantly rescued (Fig. 2-7C; also see Fig. 2-7, M, N). Note that we confirmed the expression of both mChe-DYNC2LI1(Δ302–332) and mChe-DYNC2LI1(L117V) by immunoblotting analysis of the cell lysates (Fig. 2-7O, lane 2).

We also compared the ciliary localizations of GPR161 in the presence or absence of SAG treatment in *DYNC2LI1*-KO cells expressing a combination of DYNC2LI1(Δ302–332) and either DYNC2LI1(WT) or DYNC2LI1(L117V). Again, when expressed alone in *DYNC2LI1*-KO cells, DYNC2LI1(L117V) (Fig. 2-8, D, H), but not DYNC2LI1(Δ302–332) (Fig. 2-8, A, E; also see Fig. 2-8Y), restored the ciliary exit of GPR161 in response to SAG treatment. Combinatorial expression of DYNC2LI1(Δ302–332) and DYNC2LI1(WT) also restored the exit of GRP161 from cilia upon SAG treatment (Fig. 2-8, B, F; also see Fig. 2-8Y). In striking contrast, in *DYNC2LI1*-KO cells coexpressing DYNC2LI1(Δ302–332) together with DYNC2LI1(L117V), GPR161 was significantly retained within cilia even when the cells were stimulated with SAG (Fig. 2-8, C, G; also see Fig. 2-8Y). Thus, ciliary length, ciliary localization of IFT88, and the induced exit of GPR161 were abnormal in *DYNC2LI*1-KO cells coexpressing DYNC2LI1(Δ302–332) together with the missense variant DYNC2LI1(L117V), but not together with DYNC2LI1(WT). These observations are consistent with a previous study showing that in fibroblasts derived from an SRPS individual with heterozygous alleles of DYNC2LI1(Δ302–332) and DYNC2LI1(L117V), IFT components including IFT88 were accumulated within cilia (Taylor et al., 2015).

Another case study reported an individual with skeletal ciliopathy with a spectrum between EvC and JATD caused by compound heterozygous variations of DYNC2LI1(T221I) and DYNC2LI1(1–207) (Table 2-1) (Kessler et al., 2015). A subsequent study reported EvC patients with combinations of DYNC2LI1(T221I) and either DYNC2LI1(V141*) or an initiation codon mutant of DYNC2LI1 (Table 2-1) (Niceta et al., 2018). Thus, DYNC2LI1(T221I) is likely to be crucial for the pathogenesis of EvC. We therefore analyzed the effects of the expression of DYNC2LI1(T221I) in combination with the deletion variant DYNC2LI1(1–207) in *DYNC2LI1*-KO cells. As described above (see Fig. 2-5), *DYNC2LI1*-KO cells expressing mChe-DYNC2LI1(1–207) alone demonstrated relatively long cilia with substantial accumulation of IFT88

within cilia (Fig. 2-7E), and impaired exit of GRP161 in response to SAG treatment (Fig. 2-8, I, M). On the other hand, the phenotype of *DYNC2LI1*-KO cells expressing mChe-DYNC2LI1(T221I) appeared to be normal (Fig. 2-7H, and Fig. 2-8, L, P; also see Fig. 2-7, M, N, and Fig. 2-8Z). When DYNC2LI1(1–207) was coexpressed with either DYNC2LI1(WT) or DYNC2LI1(T221I) in *DYNC2LI1*-KO cells, their phenotypes appeared to be normal (Fig. 2-7, F, G; and Fig. 2-8, J, K and N, O; also see Fig. 2-7, M, N and Fig. 2-8Z) and were indistinguishable from those expressing DYNC2LI1(WT) alone (see Figs. 2-5 and 2-6). Thus, the pathogenic combination of EvC [DYNC2LI1(1–207) and DYNC2LI1(T221I)] did not apparently affect ciliogenesis or ciliary protein localization (see Discussion).

While this study was in progress, a case study reported a combination of the DYNC2LI1 variants DYNC2LI1(P120S) and DYNC2LI1(K310*) in a fetus with SRPS-like phenotypes (Table 2-1) (Zhang et al., 2020). We therefore analyzed the effects of this combination in *DYNC2LI1*-KO cells. However, in this experiment, we used DYNC2LI1(1–317) instead of DYNC2LI1(K310*), as we thought that cells expressing DYNC2LI1(1–317) would most closely reflect the situation of those expressing DYNC2LI1(K310*). As described above (see Fig. 2-5), *DYNC2LI1*-KO cells expressing DYNC2LI1(1–317) alone demonstrated relatively short cilia, significant enrichment of IFT88 within cilia (Fig. 2-7I), and impaired exit of GPR161 in response to SAG treatment (Fig. 2-8, Q, U), whereas those expressing DYNC2LI1(P120S) were normal with respect to cilia length, IFT88 localization (Fig. 2-7L), and GPR161 exit (Fig. 2-8, T, X). *DYNC2LI1*-KO cells coexpressing DYNC2LI1(1–317) and DYNC2LI1(WT) also appeared normal regarding cilia length and IFT88 localization (Fig. 2-7J; also see Fig. 2-7, M, N) and the SAG-induced exit of GPR161 (Fig. 2-8, R, V; also see Fig. 2-8AA). However, *DYNC2LI1*-KO cells coexpressing DYNC2LI1(1–317) and DYNC2LI1(P120S) had short cilia and considerable enrichment of IFT88 within cilia (Fig. 2-7K; also see Fig. 2-7, M, N) and significant impairment of GRP161 exit upon SAG treatment (Fig. 2-8, S, W; also see Fig. 2-8AA). Thus, *DYNC2LI1*-KO cells coexpressing DYNC2LI1(1–317) together with DYNC2LI1(L117V), but not with DYNC2LI1(WT), were abnormal with regard to their cilia length, ciliary IFT88 localization, and GPR161 exit from cilia.

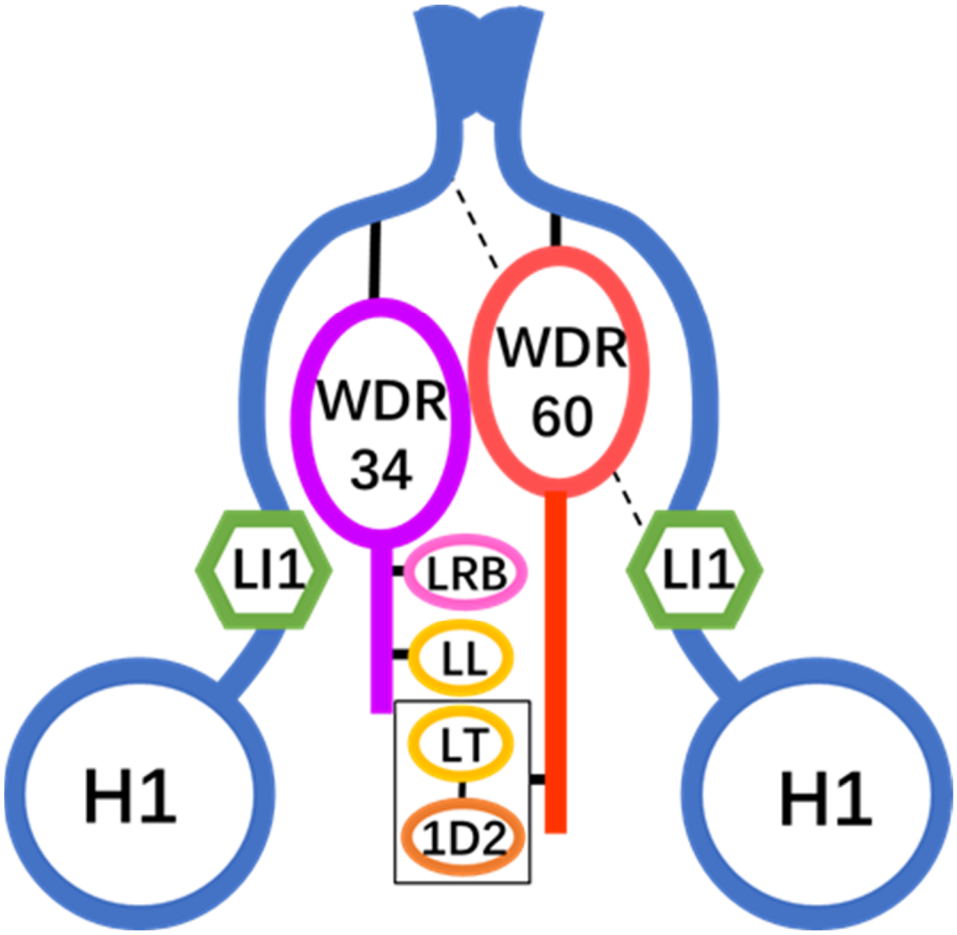

Fig. 2-1. Schematic representation of the architecture of the dynein-2 complex
The architecture of the dynein-2 complex predicted from previous studies (Hamada et al., 2018; Tsurumi et al., 2019; Toropova et al., 2019). H1, DYNC2H1; LI1, DYNC2LI1; LRB, DYNLRB; LL, DYNLL; LT, DYNLT; 1D2, TCTEX1D2. See main text for details.

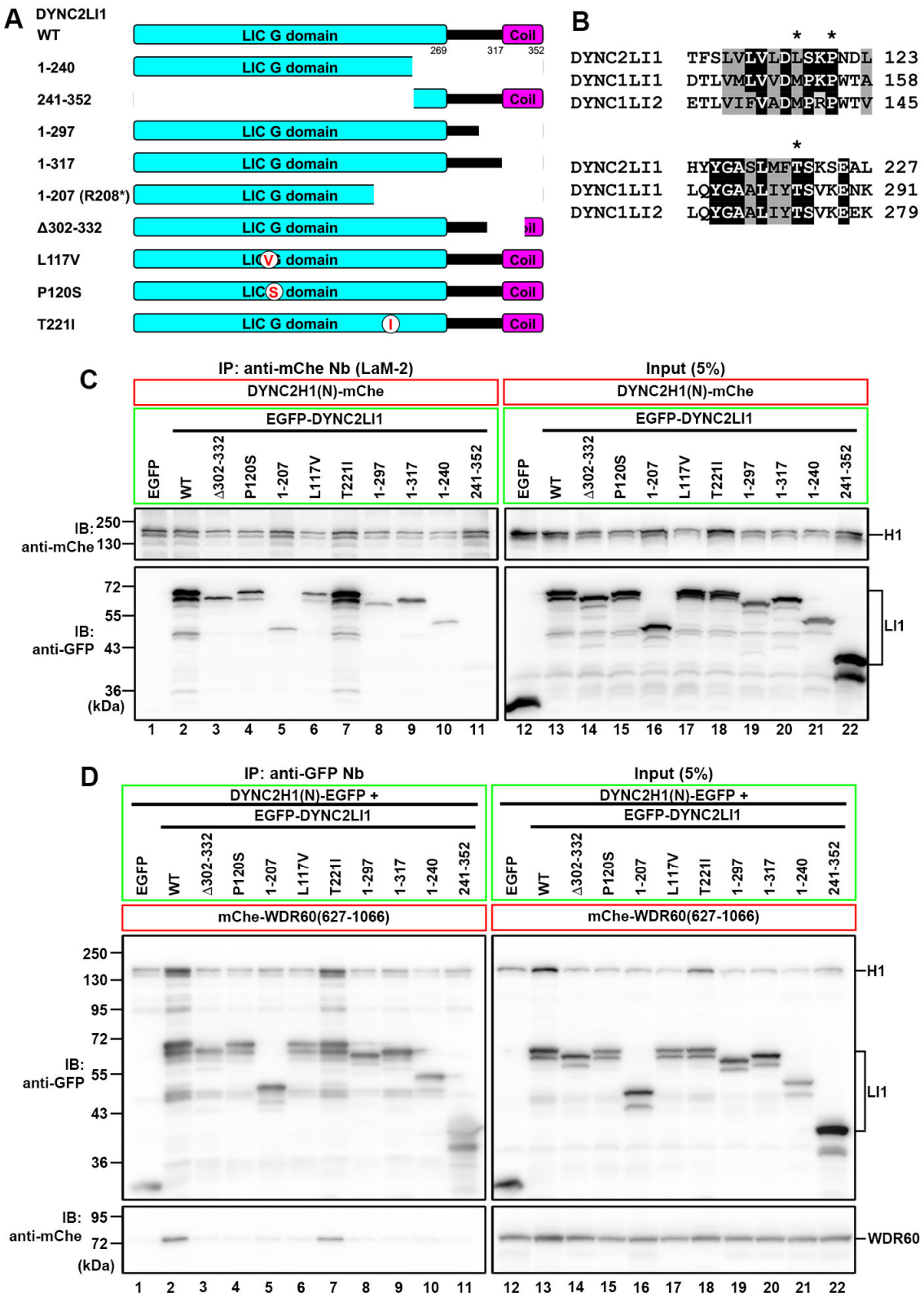
A
DYNC2LI1
WT
1-240
241-352
1-297
1-317
1-207 (R208*)
Δ302-332
L117V
P120S
T221I
LIC G domain
Coil
269
317
352
B
DYNC2LI1 TFSLVLVLDLSKPNDL 123
DYNC1LI1 DTLVMLVVDMPKPWTA 158
DYNC1LI2 ETLVIFVADMPRPWTV 145
DYNC2LI1 HYYGASIMFTSKSEAL 227
DYNC1LI1 LQYGAATIYTSVKENK 291
DYNC1LI2 LQYGAATIYTSVKEEK 279
C
IP: anti-mChe Nb (LaM-2)
Input (5%)
DYNC2H1(N)-mChe
EGFP-DYNC2LI1
EGFP
WT
Δ302-332
P120S
1-207
L117V
T221I
1-297
1-317
1-240
241-352
IB: anti-mChe
IB: anti-GFP
250
130
72
55
43
36
(kDa)
H1
LI1
1 2 3 4 5 6 7 8 9 10 11 12 13 14 15 16 17 18 19 20 21 22
D
IP: anti-GFP Nb
Input (5%)
DYNC2H1(N)-EGFP +
EGFP-DYNC2LI1
mChe-WDR60(627-1066)
IB: anti-GFP
IB: anti-mChe
95
WDR60
1 2 3 4 5 6 7 8 9 10 11 12 13 14 15 16 17 18 19 20 21 22

Fig. 2-2. Variations of DYNC2LI1 found in SRTD individuals affect its interactions with DYNC2H1 and WDR60

(A) Schematic representation of the DYNC2LI1 constructs used in the interaction experiments shown in (C, D). and in Fig. 2-3, (A, B). (B) Sequence alignment of the conserved regions among human DYNC2LI1, DYNC1LI1, and DYNC1LI2. Amino acid residues identical between DYNC2LI1 and DYNC1LI1 and/or DYNC1LI2 are shown in a black background, and those with conservative substitutions are shown in a grey background. (C) Lysates prepared from HEK293T cells coexpressing EGFP-fused DYNC2LI1 constructs, as indicated, and DYNC2H1(N)-mChe were subjected to immunoprecipitation using GST-tagged anti-mChe Nb (LaM-2 version), followed by immunoblotting analysis using anti-mChe and anti-GFP antibodies. (D) Lysates of cells coexpressing the DYNC2H1(N)-EGFP combined with EGFP-vector or EGFP-fused DYNC2LI1 constructs, as indicated, together with mChe-WDR60(627–1,066) (D), were subjected to immunoprecipitation using GST–anti-GFP Nb, followed by immunoblotting analysis using anti-mChe and anti-GFP antibodies.

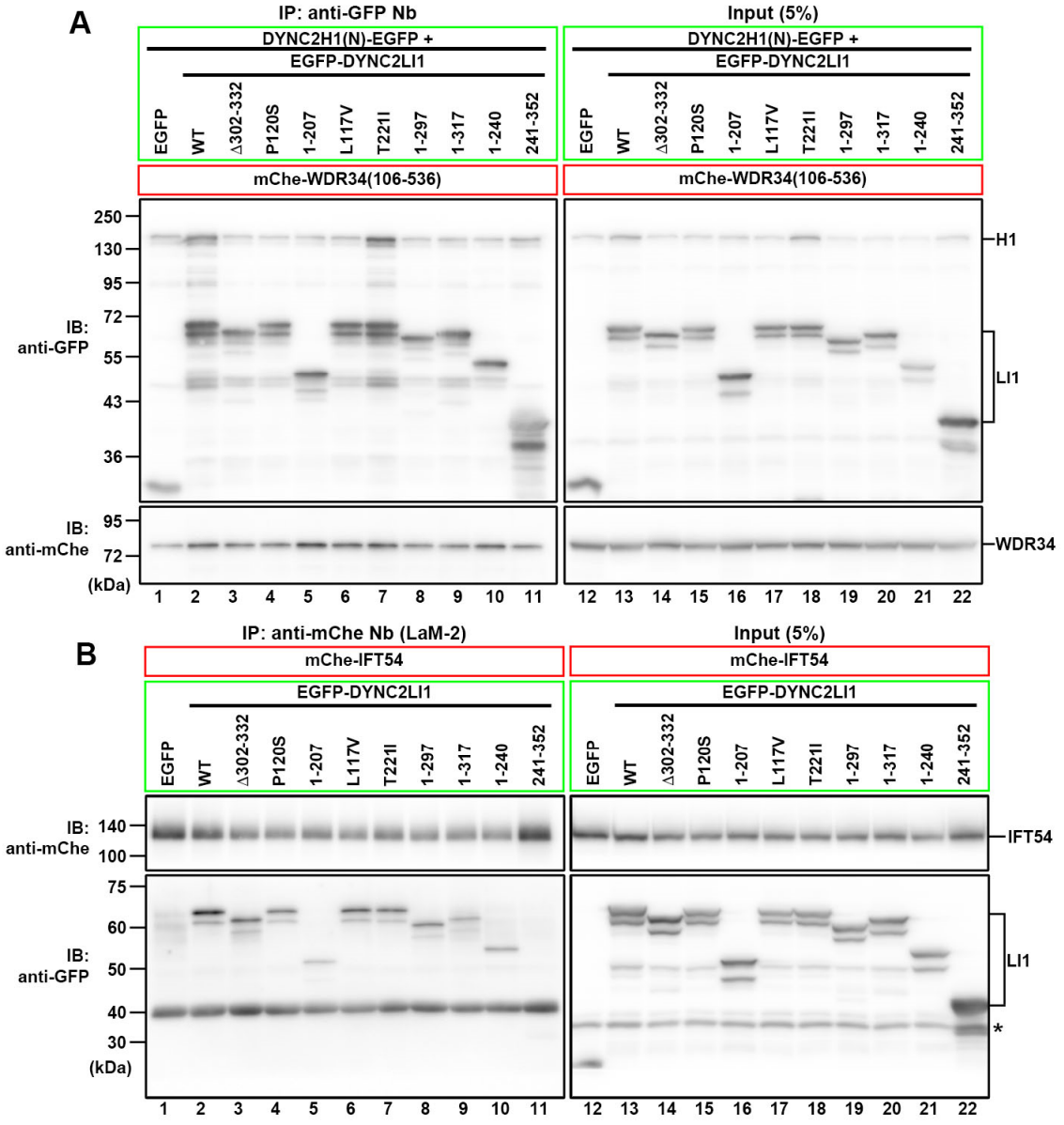

Fig. 2-3. SRTD-associated variations of DYNC2LI1 do not clearly affect its interaction with WDR34 or IFT54

(A) Lysates of cells coexpressing DYNC2H1(N)-EGFP combined with EGFP-vector or EGFP-fused DYNC2LI1 constructs, as indicated, together with mChe-WDR34(106–536), were subjected to immunoprecipitation using GST–anti-GFP Nb, followed by immunoblotting analysis using anti-mChe and anti-GFP antibodies. (B) Lysates prepared from HEK293T cells coexpressing EGFP-fused DYNC2LI1 constructs, as indicated, and mChe-IFT54 were subjected to immunoprecipitation using GST-tagged anti-mChe Nb (LaM-2 version), followed by immunoblotting analysis using anti-mChe and anti-GFP antibodies.

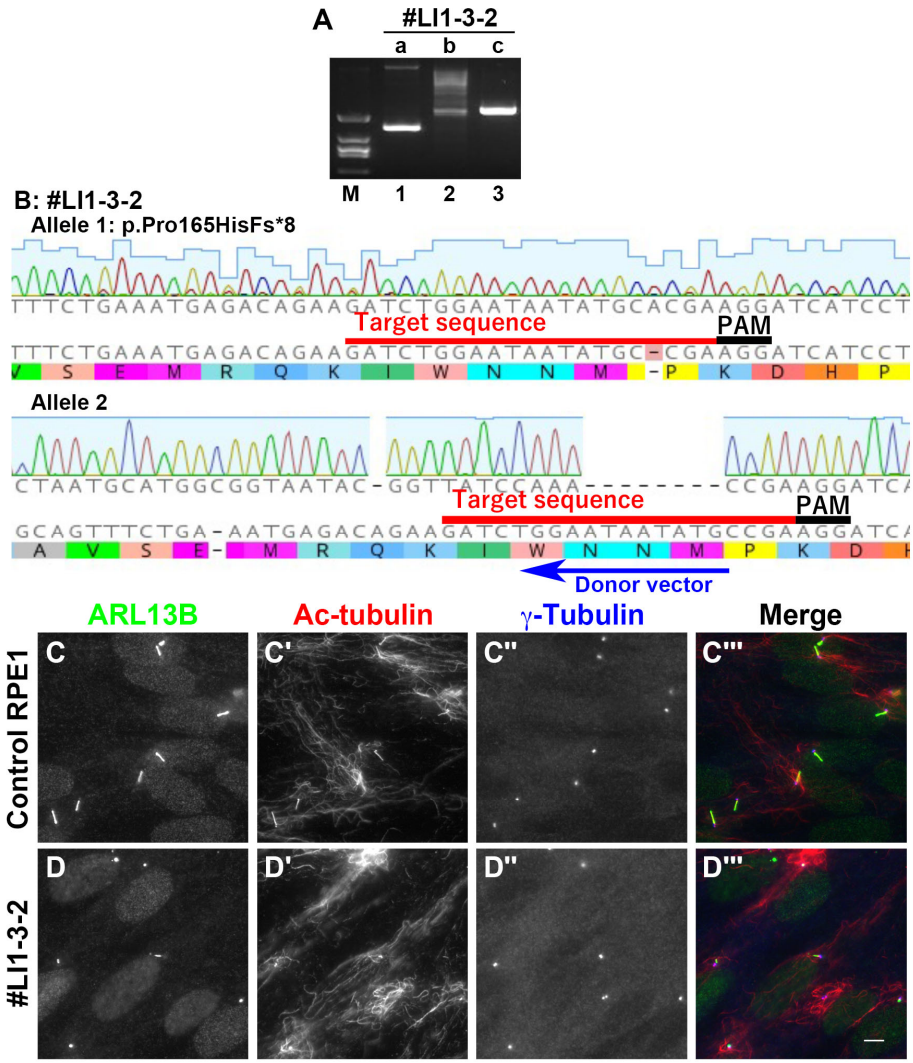

Fig. 2-4. Characterization of the *DYNC2LI1*-KO cell line

(A) Genomic DNA extracted from the *DYNC2LI1*-KO cell line #LI1-3-2 was subjected to PCR using the indicated primer pairs (see Table S2-3) to detect alleles with a small indel or no insertion (a), or with a forward (b) or reverse (c) integration of the donor knockin vector. M, molecular weight marker (pSP64 DdeI digested). (B) Alignments of allele sequences of the #LI1-3-2 cell line determined by sequencing of the PCR products shown in (A). Red and black lines indicate the target sequence and the protospacer adjacent motif (PAM) sequence, respectively, and the blue arrow indicates the direction of integration of the donor knockin vector. (C, D) Control RPE1 cells (C) and the #LI1-3-2 cell line (D) were serum-starved for 24 h to induce ciliogenesis, and triply immunostained for ARL13B, Ac-tubulin, and γ-tubulin. Scale bar, 5 μm. Note that the #LI1-3-2 cell line has very short cilia demonstrated by staining for ARL13B and Ac-tubulin.

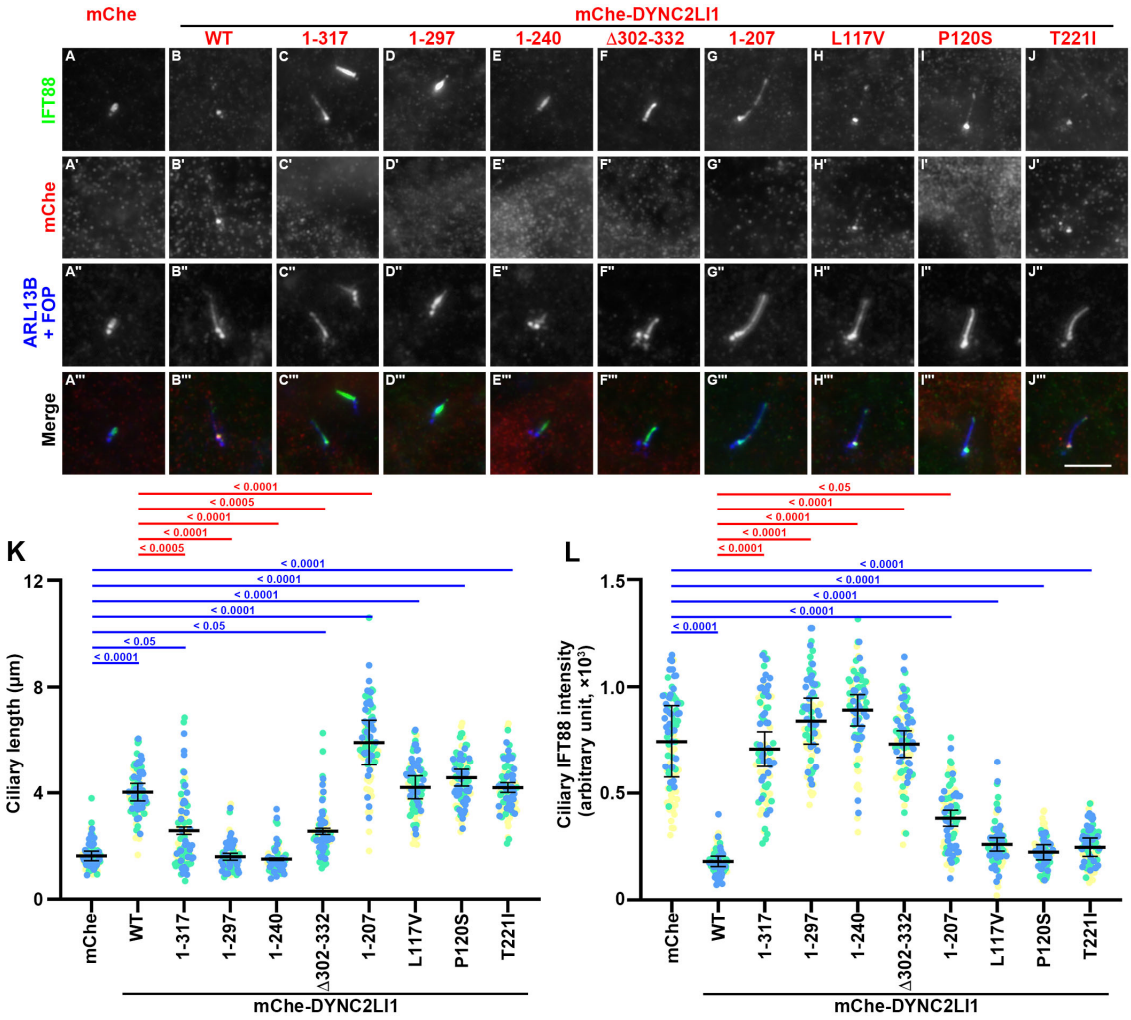

Fig. 2-5. Effects of the expression of DYNC2LI1 variants on ciliogenesis and IFT88 localization in *DYNC2LI1*-KO cells

(A–K) *DYNC2LI1*-KO cells expressing mChe (A), or mChe-fused DYNC2LI1 constructs as indicated (B–J) were serum-starved for 24 h to induce ciliogenesis, and immunostained with antibodies against IFT88 (A–J) and ARL13B+FOP (A″–J″). Scale bar, 5 μm. (K) Ciliary lengths of individual cells were measured and expressed as scatter plots. (L) Relative ciliary staining intensities of IFT88 were estimated and expressed as scatter plots. Different colored dots represent three independent experiments (n = 30 × 3). Horizontal lines are means, and error bars are SD. Statistical significances were calculated using one-way ANOVA followed by the Dunnett's multiple comparison test.

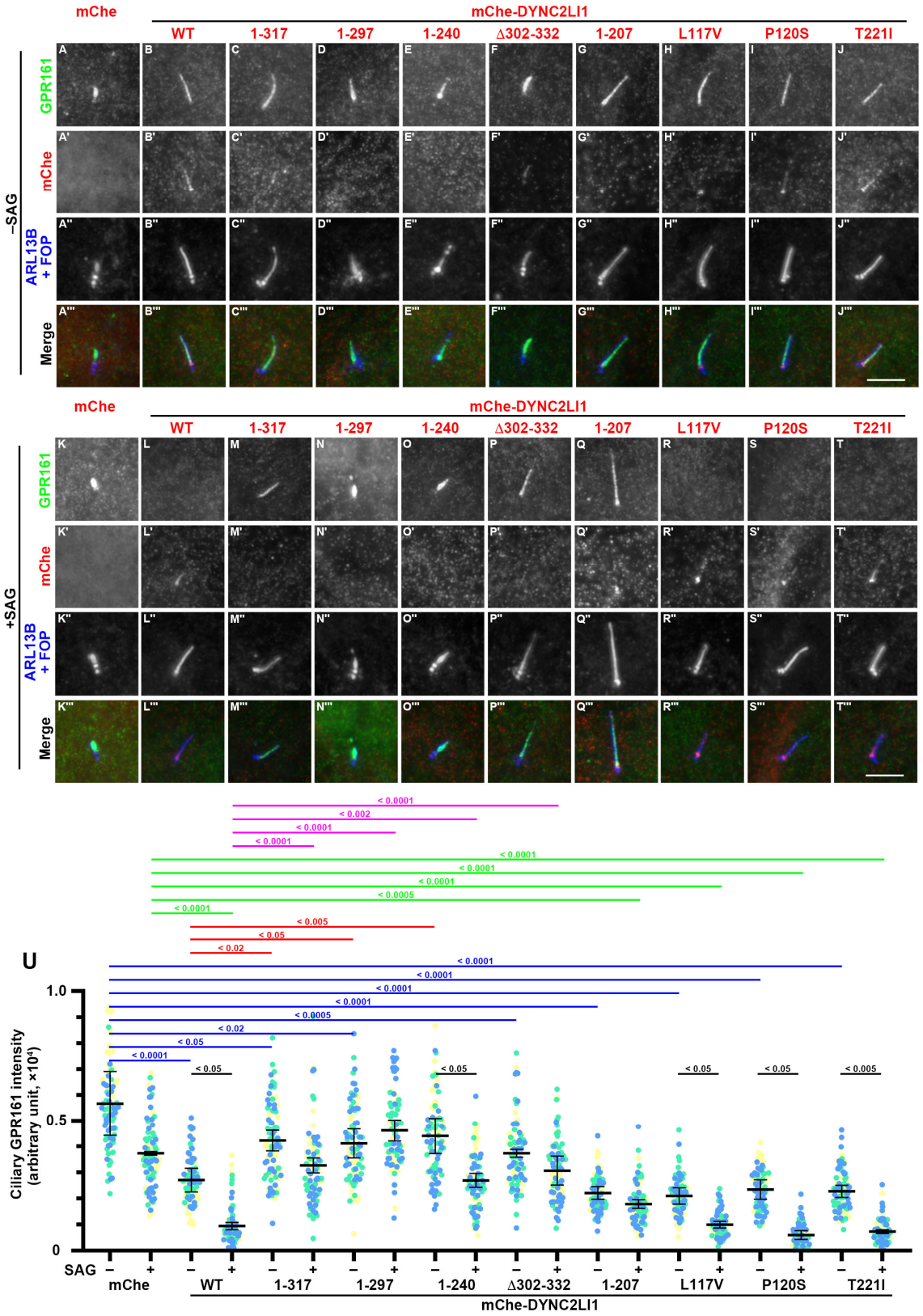
mChe
mChe-DYNC2LI1
WT
1-317
1-297
1-240
Δ302-332
1-207
L117V
P120S
T221I
−SAG
+SAG
GPR161
mChe
ARL13B + FOP
Merge
U
Ciliary GPR161 intensity (arbitrary unit, x10⁴)
1.0
0.5
0
SAG
mChe
mChe-DYNC2LI1

Fig. 2-6. Effects of the expression of DYNC2LI1 variants on basal ciliary level and induced ciliary exit of GPR161 in *DYNC2LI1*-KO cells

(A–T) *DYNC2LI1*-KO cells expressing mChe (A, K), or mChe-fused DYNC2LI1 constructs as indicated (B–J, L–T) were serum-starved for 24 h to induce ciliogenesis, cultured in the absence (A–J; –SAG) or presence (K–T; +SAG) of SAG for a further 24 h, and immunostained with antibodies against GPR161 (A–T) and ARL13B+FOP (A″–T″). Scale bars, 5 μm. (U) Relative ciliary staining intensities of GPR161 were estimated and expressed as scatter plots. Different colored dots represent three independent experiments (n = 30 × 3), horizontal lines are means, and error bars are SD. Statistical significances among multiple cell lines were calculated using one-way ANOVA followed by the Dunnett's multiple comparison test, and those between two groups (–SAG and +SAG) were calculated using the Student t-test.

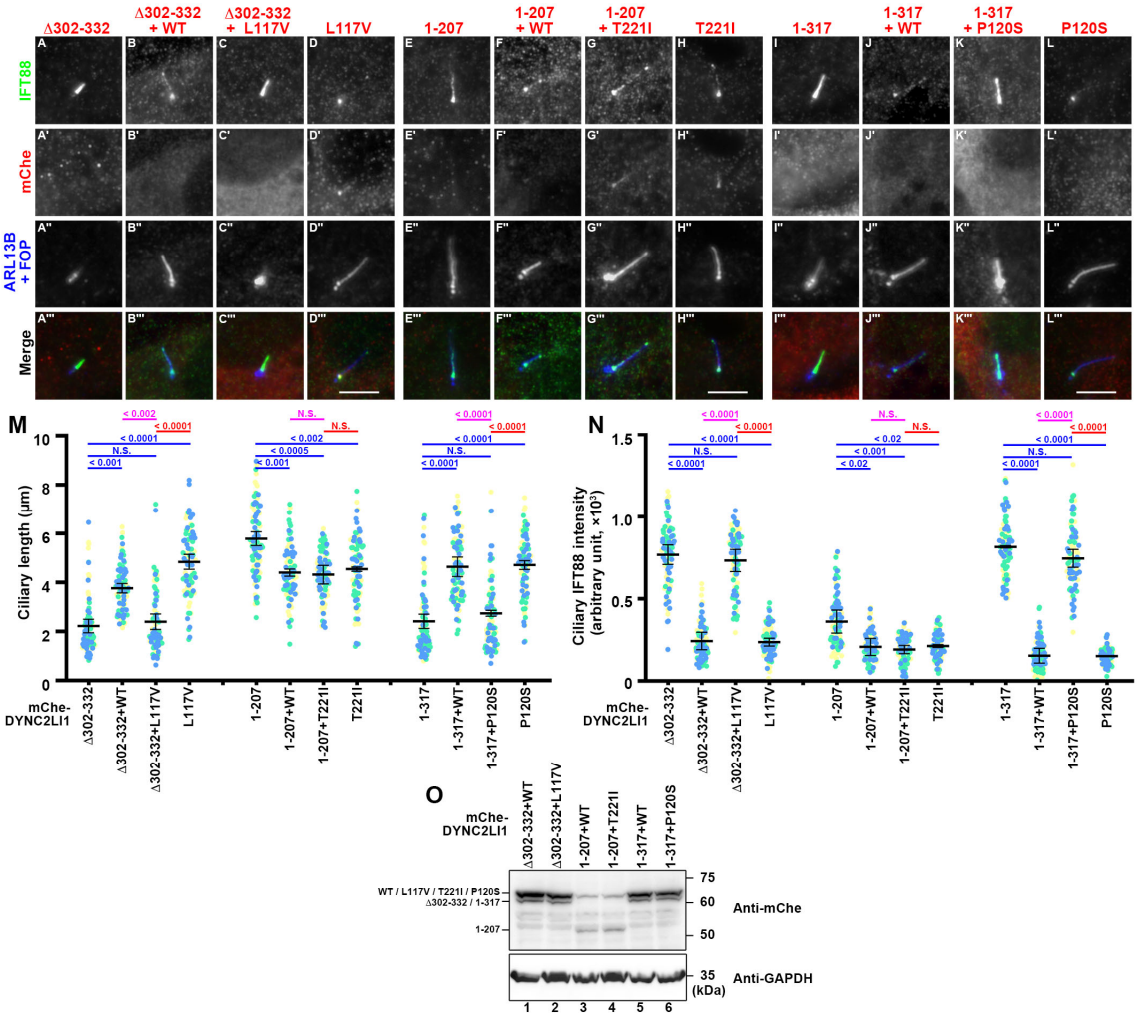

Fig. 2-7. Specific combinations of DYNC2LI1 variants are unable to rescue defects in ciliogenesis and IFT88 localization in *DYNC2LI1*-KO cells

(A–L) *DYNC2LI1*-KO cells expressing the indicated mChe-fused DYNC2LI1 construct or the indicated combinations of mChe-fused DYNC2LI1 constructs were serum-starved for 24 h and immunostained with antibodies against IFT88 (A–L) and ARL13B+FOP (A″–L″). Scale bars, 5 μm. (M, N) Ciliary lengths of individual cells and staining intensities for IFT88 in the experiments shown in (A)–(L) were measured and expressed as scatter plots, and analyzed as described in the legend to Fig. 2-5, K and L, respectively. (O) Immunoblotting analysis of equivalent amounts of cell lysates coexpressing the indicated combinations of mChe-fused DYNC2LI1 constructs, with an anti-mChe antibody.

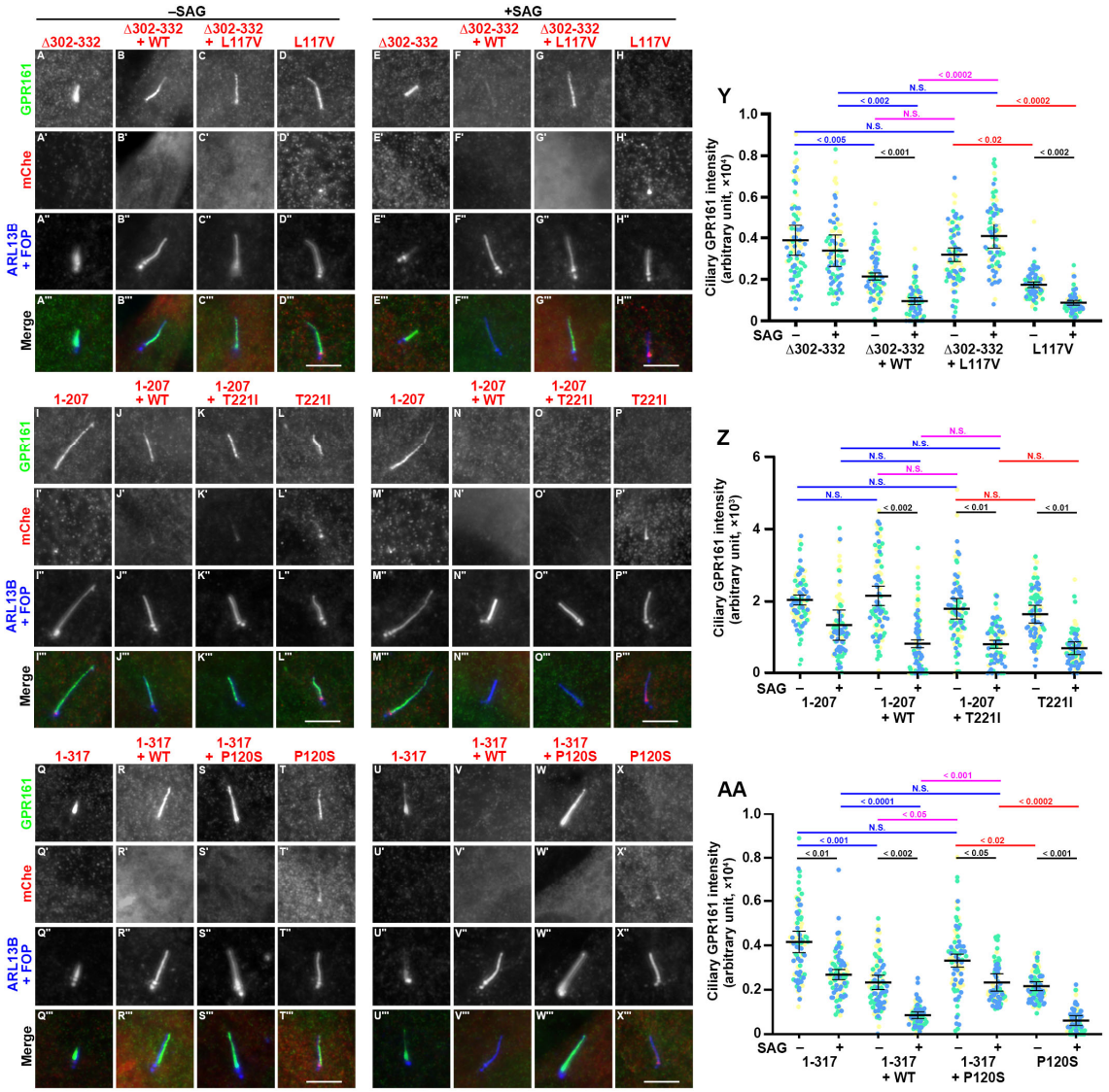

Fig. 2-8. Specific combinations of DYNC2LI1 variants are unable to rescue defects in the induced exit of GPR161 from cilia in *DYNC2LI1*-KO cells

(A–U) *DYNC2LI1*-KO cells expressing the indicated mChe-fused DYNC2LI1 construct or the indicated combinations of mChe-fused DYNC2LI1 constructs were serum-starved for 24 h to induce ciliogenesis, cultured in the absence (A–D, I–L, Q–T; –SAG) or presence (E–H, M–P, U–X; +SAG) of SAG for a further 24 h, and immunostained with antibodies against GPR161 (A–T) and ARL13B+FOP (A″–T″). Scale bars, 5 μm. (Y, Z, AA) Relative ciliary staining intensities of GPR161 in the experiments shown in A–H, I–P, and Q–X, respectively, were estimated and expressed as scatter plots, and analyzed as described in the legend to Fig. 2-6U.

Table 2-1. Pathogenic DYNC2LI1 variations identified in individuals with skeletal ciliopathies

	DNA variation	Location	Predicted amino acid change	Reference
R01-013A	c.349C>G c.996+1G>A	Exon 6 Intron 12	p.Leu117Val p.Ser302_Ile332del	Taylor et al. (2015)
R07-628A	c.349C>G c.372G>A	Exon 6 Exon 6	p.Leu117Val p.Trp124*	Taylor et al. (2015)
R03-303A	c.996+3A>G c.1003G>T	Intron 12 Exon 13	p.Ser302_Ile332del p.Glu335*	Taylor et al. (2015)
One family	c.622C>T c.662C>T	Exon 8 Exon 9	p.Arg208* p.Thr221Ile	Kessler et al. (2015)
Family 1	c.2T>C c.662C>T	Exon 1 Exon 9	p.Met1? p.Thr221Ile	Niceta et al. (2018)
Family 2	c.462delA c.662C>T	Exon 6 Exon 9	p.Val141* p.Thr221Ile	Niceta et al. (2018)
Family 3	c.123_124insA c.658-11delT	Exon 2 Intron 8	pGly42Argfs12* ?	Niceta et al. (2018)
One family	c.358C>T c.928A>T	Exon 6 Exon 12	p.Pro120Ser p.Lys310*	Zhang et al. (2020)

DISCUSSION

In this Chapter, I here demonstrated the molecular and cellular basis of the ciliary defects in SRPS skeletal ciliopathy caused by compound heterozygous variations of the dynein-2 LIC, DYNC2LI1. Namely, I showed that combinatorial expression of a DYNC2LI1 variant with an extensive deletion [DYNC2LI1(Δ302–332) or DYNC2LI1(1–317)] together with a missense variant [DYNC2LI1(L117V) or DYNC2LI1(P120S)], but not with DYNC2LI1(WT), in *DYNC2LI1*-KO cells causes defects in cilia biogenesis, retrograde trafficking of the IFT machinery, and exit of GPR161 from cilia upon stimulation of the Hh signaling pathway (Figs. 2-7 and 2-8). These observations are consistent with ciliary defects observed in fibroblasts derived from SRPS individuals (Taylor et al., 2015), and are in line with the fact that SRPS individuals with compound heterozygous variations demonstrate severe symptoms, whereas their parents with one of the variations are healthy (Taylor et al., 2015; Zhang et al., 2020). On the other hand, expression of either of the missense variants DYNC2LI1(L117V) or DYNC2LI1(P120S) in *DYNC2LI1*-KO cells was able to rescue the ciliary defects, as with DYNC2LI1(WT) (Figs. 2-7 and 2-8). However, I found that these missense variants are indeed compromised with regard to their interactions with DYNC2H1 and WDR60 (Fig. 2-2, C, D). According to the cells experiments, missense variants could only cause ciliary defects by combination with deletion variants but not with DYNC2LI1(WT) or solo expression. Thus, these missense variations might have subtle effects on the overall function of dynein-2, and lead to an abnormal ciliary phenotype in a context-dependent manner.

In contrast to the compound heterozygous variations found in SRPS individuals, the combination of an extensive deletion and a missense variation [DYNC2LI1(1–207)/DYNC2LI1(T221I)] found in EvC individuals did not lead to apparent ciliary defects when expressed in *DYNC2LI1*-KO cells. EvC appears to be a milder subtype of SRTD than SRPS; in contrast to the prenatal lethality of SRPS individuals, EvC individuals are often able to survive to adulthood. Surprisingly, even though the DYNC2LI1(T221I) variation was reported in three compounds heterozygous EvC patients (Niceta et al., 2018), I did not detect any apparent defects in the interactions of DYNC2LI1(T221I) with DYNC2H1 and WDR60, in contrast to the other missense variants analyzed, i.e., DYNC2LI1(L117V) and DYNC2LI1(P120S) (Fig. 2-2). Thus, unlike in the case of SRPS, just a subtle defect in the interaction(s) of DYNC2LI1(T221I) with some other protein(s) might affect the trafficking and/or localization of ciliary proteins, which I did not analyze, and may be responsible for the abnormalities observed

in EvC individuals. For example, to date, our research group have not been able to detect an interaction between the dynein-2 complex and the IFT-A complex, even though involvement of the IFT-A complex in retrograde trafficking driven by the dynein-2 motor entails an interaction(s) between them. Such an interaction might take place after the dynein-2 complex is transported to the ciliary tip as an anterograde IFT cargo (see below).

In addition to DYNC2LI1, variations of other dynein-2 subunits and subunits of the IFT-A complex are known to cause SRTD (Schmidts, 2014). As the IFT-A complex together with the dynein-2 complex mediates retrograde ciliary protein trafficking, impaired retrograde trafficking is implicated in the etiology of the skeletal ciliopathies. However, these are phenotypically diverse, and even in the same proteins, different variations and different combinations of variations can cause different subsets of ciliopathies. For example, our research group have recently shown that a combination of the missense variant IFT144(L710S) and the C-terminally truncated variant IFT144(1103*), a combination which is found in CED individuals (Bredrup et al., 2011), exacerbated ciliogenesis defects when expressed in *IFT144*-KO cells, whereas expression of the missense variant alone in *IFT144*-KO cells, which mimics the cellular situation of recessive retinitis pigmentosa (Coussa et al., 2013), rescued the ciliary defects, as with the expression of IFT144(WT) (Ishida et al., 2021). Thus, the severity of the autosomal recessive ciliopathies appears to be associated with context-dependent mechanisms, in which one variant can lead to severe ciliary defects in combination with a hypomorphic variant.

To achieve its function as a retrograde motor for the IFT machinery, the dynein-2 complex must be transported to the ciliary tip as an anterograde IFT cargo. The cryo-EM structure of the human dynein-2 complex, in conjunction with the cryoelectron tomographic structure of Chlamydomonas anterograde IFT trains, suggested that the dynein-2 complex and the IFT-B complex interact with each other via multiple sites (Jordan et al., 2018; Toropova et al., 2019; Webb et al., 2020). In addition, a study using Chlamydomonas demonstrated that the IFT-B subunit IFT54 directly binds to IFT dynein via its LIC subunit (Zhu et al., 2021). I here confirmed the DYNC2LI1–IFT54 interaction and that some DYNC2LI1 variants had reduced ability to interact with IFT54 (Fig. 2-3B). In view of the extensive contacts, however, there may be additional interactions between dynein-2 and the IFT-B subunits, and some ciliopathy variations of these subunits impair the dynein-2–IFT-B interactions. Furthermore, dynein-2 must be transported as an anterograde cargo in an autoinhibited state to avoid a tug-of-war between kinesin and dynein (Toropova et al., 2017; Toropova et al., 2019; Webb et al., 2020), and the above Chlamydomonas study suggested that IFT54 interacts not only with IFT dynein but also

with heterotrimeric kinesin-II. As it is possible that the short cilia phenotype may have resulted from an increased tug-of-war between kinesin and dynein, the difference between the expression of DYNC2LI1(1–317)/DYNC2LI1(1–297)/DYNC2LI1(1–240) and that of DYNC2LI1(1–207), which results in short and long cilia, respectively (Fig. 2-5), may be owing to the differential abilities of these DYNC2LI1 constructs to interfere with the autoinhibition of dynein-2. Therefore, an interesting issue to address in the future is whether variations in the dynein-2 subunits affect the autoinhibited state.

CONCLUSIONS

The summary of the results presented in this study is as follows:

Chapter 1

1. Knockout of INPP5E results in the accumulation of IFT88 (an IFT-B subunit) or IFT140 (an IFT-A subunit) within cilia.
2. Knockout of INPP5E results in a severe defect in the export of GPR161 from cilia upon the activation of Hh signaling, but does not affect ciliary entry of SMO upon the Hh signaling activation.
3. Steady-state ciliary localization of INPP5E is not crucial for its role as a modulator of ciliary function.
4. The CTS of INPP5E is required for its ciliary retention but is dispensable for its entry into cilia.

These results show that INPP5E regulates the retrograde trafficking of the IFT machinery by maintaining a distinct phosphoinositide composition on the ciliary membrane. The function of INPP5E is not dependent on its steady-state ciliary localization. Binding of INPP5E to ARL13B is essential for its steady-state localization on the ciliary membrane but is dispensable for its entry into cilia.

Chapter 2

1. Variations of DYNC2LI1 found in SRTD individuals affect its interactions with DYNC2H1 and WDR60.
2. Defects in ciliary protein trafficking in *DYNC2LI1*-KO cells was not rescued by expression of C-terminal truncation variants of DYNC2LI1 but rescued by its missense variants.
3. The pathogenic combinations of DYNC2LI1 variants cannot rescue ciliary defects in *DYNC2LI1*-KO cells.

These data indicate that SRTD variations of DYNC2LI1 substantially reduced its abilities to interact with DYNC2H1 and WDR60, which could result in formation of the unstable dynein-2 complex. Ciliary defects in *DYNC2LI1*-KO cells were restored by coexpression of one pathogenic deletion variant together with DYNC2LI1(WT), but not by that of the deletion variant in combination with a missense variant. These results demonstrate that the DYNC2LI1 deletion variants found in skeletal ciliopathies can cause ciliary defects when combined with a missense variant, whose sole expression does not cause substantial ciliary defects.

MATERIALS AND METHODS

Plasmids, antibodies, and reagents

Expression vectors for INPP5E and its mutants used in this study are listed in Table S1-1; some of them were constructed in the previous study of our research group (Nozaki et al., 2017); the INPP5E and SSTR3 cDNAs were originally provided by Tamotsu Yoshimori (Osaka University) (Hasegawa et al., 2016) and Yumiko Saito (Hiroshima University) (Nagata et al., 2013), respectively. Plasmids containing FKBP and FRB sequences were kind gifts from Takanari Inoue (Johns Hopkins University) (Komatsu et al., 2010). Point and deletion mutants of INPP5E and EGFP-INPP5E with the N-terminal FKBP sequence, and SSTR3-mChe with the C-terminal FRB sequence, were constructed using the SLiCE cloning method (Motohashi, 2015). Packaging plasmids for the production of lentiviral vectors were kind gifts from Peter McPherson (McGill University) (Thomas et al., 2009). Expression vectors for DYNC2LI1 and other dynein-2 subunits used in this study are listed in Table S2-1; some of them were constructed in previous studies of our research group (Hamada et al., 2018; Tsurumi et al., 2019).

The antibodies used in the Chapter 1 and Chapter 2 studies are listed in Tables and S1-2 and S2-2, respectively. GST-tagged anti-GFP Nb and anti-mChe Nb (LaM-2 version) prebound to glutathione–Sepharose 4B beads (GE Healthcare) were prepared as described previously (Katoh et al., 2015; Katoh et al., 2018; Ishida et al., 2021).

SAG, polyethylenimine Max, and rapamycin were purchased from Enzo Life Sciences, Polysciences, and Sigma-Aldrich, respectively.

VIP assay and immunoblotting analysis

The VIP assay and subsequent immunoblotting analysis were carried out as described previously (Katoh et al., 2015; Katoh et al., 2016) with slight modifications (Nishijima et al., 2017), as follows: HEK293T cells expressing EGFP-tagged and mChe-tagged proteins were lysed in HMDEKN cell lysis buffer (10 mM HEPES [pH 7.4], 5 mM MgSO4, 1 mM DTT, 0.5 mM EDTA, 25 mM KCl, 0.05% NP-40). Experimental details of the VIP assay have been described previously (Katoh et al., 2018).

Coimmunoprecipitation analyses

Coimmunoprecipitation analyses were performed based on the procedures previously described for the visible immunoprecipitation assay (Katoh et al., 2015; Katoh et al., 2016; Nishijima et al., 2017). In brief, approximately 1.2×10^6 HEK293T cells

(RBC2202; RIKEN BioResource Research Center) were plated onto six-well plates. The next day, cells were transfected with EGFP and mChe fusion constructs using polyethylenimine Max (20 μg) and cultured in DMEM with high glucose supplemented with 5% fetal bovine serum (FBS) for 24 h. The cells were then suspended in 250 μL of HMDEKN cell lysis buffer (10 mM HEPES [pH 7.4], 5 mM $MgSO_4$, 1 mM DTT, 0.5 mM EDTA, 25 mM KCl, and 0.05% NP-40) containing EDTA-free protease inhibitor cocktail (Nacalai Tesque), placed on ice for 20 min, and centrifuged at 16,100 × *g* for 15 min at 4 °C in a microcentrifuge. The supernatants (200 μL) were then incubated with 5 μL of GST-tagged anti-mChe Nb (LaM-2) or anti-GFP Nb prebound to glutathione–Sepharose 4B beads (GE Healthcare) at 4 °C for 1 h, or for 3 h in the IFT54 experiments. The beads were washed three times with 180 μL of lysis buffer, boiled in SDS-PAGE sample buffer, and the proteins were separated by SDS-PAGE and electroblotted onto an Immobilon-P membrane (Merck Millipore). The membrane was then blocked in 5% skimmed milk and incubated sequentially with primary antibody and peroxidase-conjugated secondary antibody. Protein bands were detected using a Chemi-Lumi One L kit (Nacalai Tesque).

Establishment of *INPP5E*-KO cell lines and *DYNC2LI1*-KO cell lines using the CRISPR/Cas9 system

The strategy for the disruption of genes in hTERT-RPE1 cells (American Type Culture Collection, CRL-4000) by the CRISPR/Cas9 system using homology-independent DNA repair was performed as described previously (Katoh et al., 2017) with slight modifications (Okazaki et al., 2020; Tsurumi et al., 2019). Briefly, single-guide RNA (sgRNA) sequences targeting the human *INPP5E* gene (see Table S1-3) or the human *DYNC2LI1* gene (see Table S2-3) were designed using CRISPOR (Haeussler et al., 2016). Double-stranded oligonucleotides for the target sequence were inserted into the all-in-one sgRNA expression vector peSpCAS9(1.1)-2×sgRNA (Addgene #80768). hTERT-RPE1 cells grown on a 12-well plate were transfected with the sgRNA vector (1 μg) and the donor knock-in vector, pDonor-tBFP-NLS-Neo(universal) (0.25 μg; Addgene #80767), using X-tremeGENE9 reagent (Roche Applied Science). After selection of the transfected cells in the presence of G418 (600 μg/mL), sorting of tBFP-positive cells was performed using the SH800S cell sorter (SONY) at the Medical Research Support Center, Graduate School of Medicine, Kyoto University. Genomic DNA extracted from the isolated cells were analyzed by PCR using GoTaq Master Mixes (Promega) and three sets of primers (Table S1-3, Table S2-3) to distinguish the following three states of integration of the donor knockin vector: forward integration, reverse integration, and no integration

with a small indel. The disruption was confirmed by direct sequencing of the PCR products.

Preparation of lentiviral vectors and cells stably expressing EGFP-fused INPP5E constructs, mChe-fused DYNC2LI1 constructs, and SSTR3-mChe-FRB

The preparation of lentiviral vectors was performed as described previously (Takahashi et al., 2012; Katoh et al., 2017). Briefly, the pRRLsinPPT-based vectors for various constructs were transfected into HEK293T cells together with the packaging plasmids [pRSV-REV, pMD2.g, and pMDLg/pRRE; kind gifts from Peter McPherson, McGill University (Thomas et al., 2009)]. The culture medium was replaced 8 h after transfection and collected between 24 to 48 h after transfection. The medium containing viral particles was passed through a 0.45-μm filter and centrifuged at 32,000 × *g* at 4 °C for 4 h. Precipitated lentiviral particles were resuspended in DMEM/F-12 and stored at −80 °C until use. Cells stably expressing the construct were prepared by the addition of the lentiviral suspension to the culture medium followed by a 24-h incubation and used for subsequent analyses.

Immunofluorescence analysis

Parental hTERT-RPE1 cells and KO cells were cultured in DMEM/F-12 supplemented with 10% FBS and 0.348% sodium bicarbonate. To induce ciliogenesis, cells were grown to 100% confluence on coverslips, and starved for 24 h in Opti-MEM (Invitrogen) containing 0.2% bovine serum albumin to induce ciliogenesis. Subsequent immunofluorescence analysis was performed as described previously (Takahashi et al., 2012; Hirano et al., 2017). The cells were fixed and permeabilized with 3% paraformaldehyde at 37 °C for 5 min, and subsequently in methanol at −20 °C for 5 min, and washed three times with phosphate-buffered saline. The fixed/permeabilized cells were blocked with 10% FBS, stained with antibodies diluted in 5% FBS, and observed using an Axio Observer microscope (Carl Zeiss). For quantification analysis, all images acquired under the same setting and saved in CZI file format were processed and analyzed by using ZEISS ZEN microscope software (Version 3.1; Carl Zeiss). A new model of cilia was created by drawing the contour of cilia along the signal of Ac-tubulin or ARL13B in object channel using the Intellesis trainable segmentation module of ZEN. After training many times, the model in the Intellesis trainable segmentation could automatically recognize most cilia. After manually excluding regions that were incorrectly identified as cilia, the Image Analysis application was able to use the model to automeasure ciliary length and the mean fluorescence intensity within cilia. To correct for local background

intensity, the ROI was set to a nearby region. Statistical analyses were performed using GraphPad Prism8 (Version 8.4.3; GraphPad Software, Inc.).

Table S1-1. Plasmids used in Chapter 1

Vector	Insert	Reference
pCAG2-EGFP-C	INPP5E	(Nozaki et al., 2017)
pCAG2-mCherry-N	ARL13B	(Nozaki et al., 2017)
pCAG2-EGFP-C	INPP5E(D477N)	This study
pCAG2-EGFP-C	INPP5E(ΔCTS)	This study
pRRLsinPPT-EGFP-C-IRES-Zeo	INPP5E	This study
pRRLsinPPT-EGFP-C-IRES-Zeo	INPP5E(D477N)	This study
pRRLsinPPT-EGFP-C-IRES-Zeo	INPP5E(ΔCTS)	This study
pRRLsinPPT-EGFP-C-IRES-Zeo	TULP3	(Nozaki et al., 2017)
pRRLsinPPT-EGFP-C-IRES-Blast	MKS1	(Okazaki et al., 2020)
pRRLsinPPT-mCh-FRB-N-IRES-Zeo	SSTR3	This study
pRRLsinPPT-FKBP-EGFP-C-IRES-Zeo	INPP5E	This study
pRRLsinPPT-FKBP-EGFP-C-IRES-Zeo	INPP5E(ΔCTS)	This study
pGEX-6P1	Anti-GFP-nanobody	(Katoh et al., 2015)

Table S1-2. Antibodies used in Chapter 1

Antibody	Manufacturer	Clone/catalog number or reference number	Dilution (purpose)
Polyclonal rabbit anti-IFT88	Proteintech	13967-1-AP	1:500 (IF)
Polyclonal rabbit anti-IFT140	Proteintech	17460-1-AP	1:500 (IF)
Polyclonal rabbit anti-ARL13B	Proteintech	17711-1-AP	1:1,000 (IF)
Polyclonal rabbit anti-INPP5E	Proteintech	17797-1-AP	1:500 (IF)
Polyclonal rabbit anti-GPR161	Proteintech	13398-1-AP	1:500 (IF)
Polyclonal rabbit anti-TCTN1	Proteintech	15004-1-AP	1:100 (IF)
Monoclonal mouse anti-ARL13B	Abcam	N295B/66	1:500 (IF)
Monoclonal mouse anti-SMO	Santa Cruz	sc-166685	1:100 (IF)
Monoclonal mouse anti-Ac-tubulin	Sigma-Aldrich	6-11B-1	1:1,000 (IF)
Monoclonal mouse anti-γ-tubulin	Sigma-Aldrich	GTU88	1:500 (IF)
Monoclonal mouse anti-polyglutamylation modification	AdipoGen	GT335	1:500 (IF)
Monoclonal mouse anti-FOP	Abnova	2B1	1:10,000 (IF)
Polyclonal rabbit anti-GFP	Invitrogen	A11122	1:10,000 (IF)
Polyclonal rabbit anti-mCherry	Proteintech	26765-1-AP	1:10,000 (IB)
Monoclonal mouse anti-GFP	Proteintech	66002-1-Ig	1:10,000 (IB)
AlexaFluor-conjugated secondary	Molecular Probes	A11034, A27039, A21244,	1:1,000 (IF)

		A11004, A21127, A21240, A21241, A21131, A21242	
Peroxidase-conjugated secondary	Jackson ImmunoResearch	115-035-166, 111-035-144	1:3,000 (IB)

IF, immunofluorescence; IB, immunoblotting

Table S1-3. Oligo DNAs used in Chapter 1

Name	Sequence
INPP5E -genome-FW (primer 1)	5'- CGTCCAAGGCGGAGAATCTG-3'
INPP5E -genome-RV (primer 2)	5'- TTGTAGTCTGCAAGATCCGAGTC-3'
pTagBFP-N-RV2 (primer 3)	5'- CGTAGAGGAAGCTAGTAGCCAGG -3'
SLiCE-INPP5E-D477N-S	5'- GGTTTGGAAACTTCAACTTCCGCCTG-3'
SLiCE-INPP5E-D477N-AS	5'- GTTGAAGTTTCCAAACCAGAACACCTC-3'
SLiCE-INPP5E-delCTS-S	5'- AGCTGGGCAAACTAGGAATTAAAAGACGGATTTC-3'
SLiCE-INPP5E-delCTS-AS	5'-TAATTCCTAGTTTGCCAGCTGCCAAC-3'
SLiCE-IRES-FKBP-S	5'-GATGATAAGCTTGCCACAAGCCACCATGGGAGTGCAG-3'
SLiCE-IRES-INPP5E-AS	5'-TGTAATCCAGAGGTTGATTTCAAGAAACGGAGCAGATGG-3'
INPP5E-gRNA#1-S	5'- CACCCCTGGACCCCGATGACATAC-3'
INPP5E-gRNA#1-AS	5'- AAACGTATGTCATCGGGGTCCAGG-3'
INPP5E-gRNA#2-S	5'- CACCGGAAATCCCCAAGTCCCGCG-3'
INPP5E-gRNA#2-AS	5'- AAACCGCGGGACTTGGGGATTTCC-3'

Table S2-1. Plasmids used in Chapter 2

Vector	Insert	Reference
pCAG2-EGFP-C	DYNC2LI1	Hamada et al., 2018
pCAG2- mCherry-C	WDR34(106–536)	Tsurumi et al., 2019
pCAG2-EGFP-N	DYNC2H1(N; 1–1,090)	This study
pCAG2-mCherry-N	DYNC2H1(N; 1–1,090)	This study
pCAG2- mCherry-C	WDR60(627–1,066)	This study
pCAG2- mCherry-C	IFT54	This study
pCAG2-EGFP-C	DYNC2LI1(Δ302–332)	This study
pCAG2-EGFP-C	DYNC2LI1(P120S)	This study
pCAG2-EGFP-C	DYNC2LI1(1-207)	This study
pCAG2-EGFP-C	DYNC2LI1(L117V)	This study
pCAG2-EGFP-C	DYNC2LI1(T221I)	This study
pCAG2-EGFP-C	DYNC2LI1(1–297)	This study
pCAG2-EGFP-C	DYNC2LI1(1–317)	This study
pCAG2-EGFP-C	DYNC2LI1(1–240)	This study
pCAG2-EGFP-C	DYNC2LI1(241–352)	This study
pRRLsinPPT-mCherry-C-IRES-Zeo	DYNC2LI1	Hamada et al., 2018
pRRLsinPPT-mCherry-C-IRES-Zeo	DYNC2LI1(Δ302–332)	This study
pRRLsinPPT-mCherry-C-IRES-Zeo	DYNC2LI1(P120S)	This study
pRRLsinPPT-mCherry-C-IRES-Zeo	DYNC2LI1(1–207)	This study
pRRLsinPPT-mCherry-C-IRES-Zeo	DYNC2LI1(L117V)	This study
pRRLsinPPT-mCherry-C-IRES-Zeo	DYNC2LI1(T221I)	This study
pRRLsinPPT-mCherry-C-IRES-Zeo	DYNC2LI1(1–297)	This study
pRRLsinPPT-mCherry-C-IRES-Zeo	DYNC2LI1(1–317)	This study
pRRLsinPPT-mCherry-C-IRES-Zeo	DYNC2LI1(1–240)	This study
pDonor-tBFP-NLS-Neo (Universal)	–	Katoh et al., 2017
peSpCas9 (1.1)-2×gRNA	–	Katoh et al., 2017
pGEX-6P1	Anti-GFP-nanobody	Katoh et al., 2015
pGEX-6P1	Anti-mCherry-Nanobody (LaM-2)	Ishida et al., 2021

Table S2-2. Antibodies used in Chapter 2

Antibody	Manufacturer	Clone/catalog number or reference number	Dilution (purpose)
Polyclonal rabbit anti-IFT88	Proteintech	13967-1-AP	1:500 (IF)
Polyclonal rabbit anti-GPR161	Proteintech	13398-1-AP	1:500 (IF)
Polyclonal rabbit anti-ARL13B	Proteintech	17711-1-AP	1:500 (IF)
Monoclonal mouse anti-ARL13B	Abcam	N295B/66	1:500 (IF)
Monoclonal mouse anti-FOP	Abnova	2B1	1:10,000 (IF)

Monoclonal mouse anti-Ac-α-tubulin	Sigma-Aldrich	6-11B-1	1:1,000 (IF)
Monoclonal mouse anti-γ-tubulin	Sigma-Aldrich	GTU88	1:1,000 (IF)
Monoclonal mouse anti-RFP	MBL	3G5	1:1,000 (IF)
Polyclonal rabbit anti-mCherry	Proteintech	26765-1-AP	1:10,000 (IB)
Monoclonal mouse anti-GFP	Proteintech	66002-1-Ig	1:10,000 (IB)
Monoclonal mouse anti-GAPDH	Ambion	6C5	1:10,000 (IB)
AlexaFluor-conjugated secondary	Molecular Probes	A11034, A27039, A21244, A11004, A21127, A21240, A21241, A21131, A21242	1:1,000 (IF)
Peroxidase-conjugated secondary	Jackson ImmunoResearch	115-035-166, 111-035-144	1:3,000 (IB)

IF, immunofluorescence; IB, immunoblotting

Table S2-3. Oligo DNAs used in Chapter 2

Name	Sequence
pTagBFP-N-RV2 (primer 3)	5'-CGTAGAGGAAGCTAGTAGCCAGG-3'
DYNC2LI1-genome#1-FW (primer 1)	5'- GGTCATCTGGTTAAAGTGTTGAAGT-3'
DYNC2LI1-genome#1-RV (primer 2)	5'- GGGCTGTGGTCACCCCAGAC-3'
DYNC2LI1-genome#2-FW (primer 4)	5'- TGATGCATTTTGAGGGATGGGA-3'
DYNC2LI1-genome#2-RV (primer 5)	5'- TATCTCAGTTCAGCACGGGC-3'
DYNC2LI1-genome#1-FW (primer 6)	5'- TCGATGCAAATGCTTGGAGC-3'
DYNC2LI1-genome#1-FW (primer 7)	5'- CCTTGTTTTGCTCTTACTGAGGT-3'
DYNC2LI1-gRNA#1-S	5'- CACCGCTTCATTGGCAGTAAAAATG-3'
DYNC2LI1-gRNA#1-AS	5'- AAACCATTTTTACTGCCAATGAAGC-3'
DYNC2LI1-gRNA#2-S	5'- CACCGCTCACTTTTGGGAACTCGG-3'
DYNC2LI1-gRNA#2-AS	5'- AAACCCGAGTTCCCAAAAGTGAGC-3'
DYNC2LI1-gRNA#3-S	5'- CACCGATCTGGAATAATATGCCGA-3'
DYNC2LI1-gRNA#3-AS	5'- AAACTCGGCATATTATTCCAGATC-3'
SLiCE-EcoRI-DYNC2LI1-FW	5'- CTCGAGCTCAAGCTTCGAATTCTATGCCCAGTGAAACTCTCTGGG-3'
SLiCE-SalI-DYNC2LI1-RV	5'- CCGGGCCCGCGGTACCGTCGACTCAAGAATCAAGCTCGATTTGTTTC-3'

SLiCE-pRRL-DYNC2LI1-S	5'- AAGTCCGGCCGGACTCAGGTTATGCCCAGTGAAACTCTCTG-3'
SLiCE-pRRL-DYNC2LI1-AS	5'- TCCAGCACACTGGATCACTCGACTCAAGAATCAAGCTC-3'
SLICE-SalI-DYNC2LI1-240aa-RV	5'-CCCGGGCCCGCGGTACCGTCGACTCAAAATGCCAACTGGTTGATAACTCC-3'
SLICE-EcoRI-DYNC2LI1-241aa-FW	5'-TCTCGAGCTCAAGCTTCGAATTCTGGCATTGACAAAAGCAAATCAATA-3'
DYNC2LI1-L117V-FW	5'- GTTCTGGATGTTTCAAAACCTAATGATCTC-3'
DYNC2LI1-L117V-RV	5'- GTTTTGAAACATCCAGAACGAGAACAAGAG-3'
DYNC2LI1-T221I-FW	5'- AATGTTTATCAGTAAATCAGAAGCTCTATTAC-3'
DYNC2LI1-T221I-RV	5'- GATTTACTGATAAACATTAATGATGCTCC-3'
SLiCE-SalI-DYNC2LI1-297aa-RV	5'- CCGGGCCCGCGGTACCGTCGACTCAGAGCTTTTCATACACTTTTTTCC-3'
SLiCE-SalI-DYNC2LI1-317aa-RV	5'- CCGGGCCCGCGGTACCGTCGACTCACTGAGGATCTCTCGCAGGGTCC-3'
SLiCE-DYNC2LI1-△Exon12-FW	5'- AGTGTATGAAAAGCTCTTTCCACCAAAGGAACTGGAACAG-3'
SLiCE-DYNC2LI1-△Exon12-RV	5'- GTTCCAGTTCCTTTGGTGGAAAGAGCTTTTCATACACTTT-3'
SLiCE-DYNC2LI1-P120S-FW	5'- CTTTCAAAATCTAATGATCTCTGGCCCACCATGGA-3'
SLiCE-DYNC2LI1-P120S-RV	5'- GAGATCATTAGATTTTGAAAGATCCAGAACGAGAACAAGAG-3'
SLiCE-DYNC2LI1-R208X-FW	5'- AAGACACTTTGATTTGTTGCACATTATTATGGAGC-3'
SLiCE-DYNC2LI1-R208X-RV	5'- GCAACAAATCAAAGTGTCTTGCATATTACCTTTCTCTTCT-3'
SLiCE-pRRL-DYNC2LI1-240aa-AS	5'-CCAGCACACTGGATCACTCGACTCAAAATGCCAACTGGTTGATAACTCC-3'
SLiCE-pRRL-DYNC2LI1-2970aa-AS	5'- CCAGCACACTGGATCACTCGACTCAGAGCTTTTCATACACTTTTTTCC-3'
SLiCE-pRRL-DYNC2LI1-317aa-AS	5'- CCAGCACACTGGATCACTCGACTCACTGAGGATCTCTCGCAGGGTCC-3'

FW, forward; RV, reverse; S, sense; AS, antisense

ACKNOWLEDGEMENTS

First of all, I would like to express my sincere gratitude to Professor Kazuhisa Nakayama, Graduate School of Pharmaceutical Sciences, Kyoto University, and Senior Lecturer Yohei Katoh, Graduate School of Pharmaceutical Sciences, Kyoto University, for their patient instruction and constructive suggestions during the course of my study.

I am deeply grateful to Dr. Shohei Nozaki, Ms. Sayaka Fujisawa, Mr. Takuya Kobayashi, Mr. Kentaro Nakamura and Ms. Zhuang Zhou for technical supports and helpful discussions.

I would like to express my gratitude to Dr. Hye-Won Shin, Dr. Hiroyuki Takatsu, Ms. Luxiaoxue Liang, Mr. Yuta Tsurumi, Mr. Takuya Tone, Ms. Misato Okazaki, Mr. Tatsuro Noguchi, Mr. Yamato Ishida, Mr. Shunya Hiyamizu and Mr. Yuuki Satoda for their technical advice and helpful discussions.

Particular thanks go to all the former and present members of the Department of Physiological Chemistry, Graduate School of Pharmaceutical Sciences, Kyoto University, for their continuous encouragements, helpful discussions, instruction and generous supports.

I also want to thank the Otsuka Toshimi Scholarship Foundation for the financial and moral support.

Finally, special thanks to my wife, my family, and my friends, who have helped me and shared with me my worries, frustrations, and happiness.

REFERENCES

Arts, H., and Knoers, N. (2013 [updated 2018]). Cranioectodermal dysplasia. In: GeneReviews® [Internet], eds. M.P. Adam, H.H. Ardinger, R.A. Pagon, S.E. Wallace, L.J.H. Bean, K. Stephens, and A. Amemiya, Seatle (WA): University of Washington.

Asante, D., Stevenson, N.L., and Stephens, D.J. (2014). Subunit composition of the human cytoplasmic dynein-2 complex. J. Cell Sci. 127, 4774-4787.

Badgandi, H. B., Hwang, S., Shimada, I. S., Loriot, E. and Mukhopadhyay, S. (2017). Tubby family proteins are adaptors for ciliary trafficking of integral membrane proteins. J. Cell Biol. 216, 743-760.

Bangs, F. and Anderson, K. V. (2017). Primary cilia and mammalian hedgehog signaling. Cold Spring Harb. Perspect. Biol. 9, a028175.

Berbari, N. F., Johnson, A. D., Lewis, J. S., Askwith, C. C. and Mykytyn, K. (2008). Identification of ciliary localization sequences within the third intracellular loop of G protein-coupled receptors. Mol. Biol. Cell 19, 1540-1547.

Bielas, S. L., Silhavy, J. L., Brancati, F., Kisseleva, M. V., Al-Gazali, L., Sztriha, L., Bayoumi, R. A., Zaki, M. S., Abdel-Aleem, A., Rosti, R. O. et al. (2009). Mutations in INPP5E, encoding inositol polyphosphate-5-phosphatase E, link phosphatidyl inositol signaling to the ciliopathies. Nat. Genet. 41, 1032-1036.

Braun, D. A. and Hildebrandt, F. (2017). Ciliopathies. Cold Spring Harb. Perspect. Biol. 9, a028191

Bredrup, C., Saunier, S., Oud, M.M., Piskerstrand, T., Hoischen, A., Brackman, D., Leh, S.M., Midtbø, M., Filhol, E., Bole-Feysot, C., Nitschké, P., Gilissen, C., Haugen, O.H., Sanders, J.-S.F., Stolte-Dijkstra, I., Mans, D.A., Steenbergen, E.J., Hamel, B.C.J., Matignon, M., Pfundt, R., Jeanpierre, C., Boman, H., Rødahl, E., Veltman, J.A., Knappskog, P.M., Knoers, N.V.A.M., Roepman, R., and Arts, H.H. (2011). Ciliopathies with skeletal anomalies and renal insufficiency due to mutations in the IFT-A gene WDR19. Am. J. Hum. Genet. 89, 634-643.

Breslow, D. K., Koslover, E. F., Seydel, F., Spakowitz, A. J. and Nachury, M. V. (2013). An in vitro assay for entry into cilia reveals unique properties of the soluble diffusion barrier. J. Cell Biol. 203, 129-147.

Briscoe, J. and Thérond, P. P. (2013). The mechanisms of Hedgehog signalling and its roles in development and disease. Nat. Rev. Mol. Cell Biol. 14, 416-429.

Chávez, M., Ena, S., Van Sande, J., de Kerchove d'Exaerde, A., Schurmans, S. and Schiffmann, S. N. (2015). Modulation of ciliary phosphoinositide content regulates trafficking and sonic hedgehog signaling output. Dev. Cell 34, 338-350.

Conduit, S. E. and Vanhaesebroeck, B. (2020). Phosphoinositide lipids in primary cilia biology. Biochem. J. 477, 3541-3565.

Corés, C.R., Metzis, V., and Wicking, C. (2015). Unmasking the ciliopathies: craniofacial

defects and the primary cilium. Wiley Interdiscip. Rev. Dev. Biol. 4, 637-653.
Coussa, R.G., Otto, E.A., Gee, H.-Y., Arthurs, P., Ren, H., Lopez, I., Keser, V., Fu, Q., Faingold, R., Khan, A.H., Schwartzentruber, J., Majewski, J., Hildebrandt, F., and Koenekoop, R.K. (2013). WDR19: an ancient, retrograde, intraflagellar ciliary protein is mutated in autosomal recessive retinitis pigentosa and in Senior-Loken syndrome. Clin. Genet. 84, 150-159.
Dutta, N. and Seo, S. (2016). RPGR, a prenylated retinal ciliopathy protein, is targeted to cilia in a prenylation- and PDE6D-depenent manner. Biol. Open 5, 1283-1289.
Dyson, J. M., Conduit, S. E., Feeney, S. J., Hakim, S., DiTommaso, T., Fulcher, A. J., Sriratana, A., Ramm, G., Horan, K. A., Gurung, R. et al. (2017). INPP5E regulates phosphoinositide-dependent cilia transition zone function. J. Cell Biol. 216, 247-263.
Eguether, T., San Agustin, J. T., Keady, B. T., Jonassen, J. A., Liang, Y., Francis, R., Tobita, K., Johnson, C. A., Abdelhamed, Z. A., Lo, C. W. et al. (2014). IFT27 links the BBSome to IFT for maintenance of the ciliary signaling compartment. Dev. Cell 21, 279-290.
Fansa, E. K. and Wittinghofer, A. (2016). Sorting of lipidated cargo by the Arl2/Arl3 system. Small GTPases 7, 222-230.
Fansa, E. K., Kösling, S. K., Zent, E., Wittinghofer, A. and Ismail, S. (2016). PDE6δ-mediated sorting of INPP5E into the cilium is determined by cargo-carrier affinity. Nat. Commun. 7, 11366.
Fisher, S., Kuna, D., Caspary, T., Kahn, R. A. and Sztul, E. (2020). ARF family GTPases with links to cilia. Am. J. Physiol. Cell Physiol. 319, C404-C418.
Garcia-Gonzalo, F. R. and Reiter, J. F. (2017). Open sesame: how transition fibers and the transition zone control ciliary composition. Cold Spring Harb. Perspect. Biol. 9, a028134.
Garcia-Gonzalo, F. R., Phua, S. C., Roberson, E. C., Garcia, G., III, Abedin, M., Schurmans, S., Inoue, T. and Reiter, J. F. (2015). Phosphoinositides regulate ciliary protein trafficking to modulate Hedgehog signaling. Dev. Cell 34, 400-409.
Gigante, E. D. and Caspary, T. (2020). Signaling in the primary cilum through the lens of the Hedgehog pathway. Wiley Interdiscip. Rev. Dev. Biol. 9, e377.
Gigante, E. D., Taylor, M. R., Ivanova, A. A., Kahn, R. A. and Caspary, T. (2020). ARL13B regulates sonic hedgehog signaling from outside primary cilia. eLife 9, e50434.
Gonçalves, J. and Pelletier, L. (2017). The ciliary transition zone: finding the pieces and assembling the gate. Mol. Cells 40, 243-253.
Gotthardt, K., Lokaj, M., Koerner, C., Falk, N., Gießl, A. and Wittinghofer, A. (2015). A G-protein activation cascade from Arl13B to Arl3 and implications for ciliary targeting of lipidated proteins. eLife 4, e11859.
Haeussler, M., Schönig, K., Eckert, H., Eschstruth, A., Mianné, J., Renaud, J.B., Schneider-Maunoury, S., Shkumatava, A., Teboul, L., Kent, J., Joly, J.S., and

Concordet, J.P. (2016). Evaluation of off-target and on-target scoring algorithms and integration into the guide RNA selection tool CRISPOR. Genome Biol. 17, 148.

Hamada, Y., Tsurumi, Y., Nozaki, S., Katoh, Y., and Nakayama, K. (2018). Interaction of WDR60 intermediate chain with TCTEX1D2 light chain of the dynein-2 complex is crucial for ciliary protein trafficking. Mol. Biol. Cell 29, 1628-1639.

Hasegawa, J., Iwamoto, R., Otomo, T., Nezu, A., Hamasaki, M. and Yoshimori, T. (2016). Autophagosome-lysosome fusion in neurons requires INPP5E, a protein associated with Joubert syndrome. EMBO J. 35, 1853-1867.

Higginbotham, H., Eom, T.-Y., Mariani, L. E., Bachleda, A., Hirt, J., Gukassyan, V., Cusack, C. L., Lai, C., Caspary, T. and Anton, E. S. (2012). Arl13b in primary cilia regulates the migration and placement of interneurons in the developing cerebral cortex. Dev. Cell 23, 925-938.

Hirano, T., Katoh, Y. and Nakayama, K. (2017). Intraflagellar transport-A complex mediates ciliary entry as well as retrograde trafficking of ciliary G protein-coupled receptors. Mol. Biol. Cell 28, 429-439.

Hirokawa, N., Niwa, S., and Tanaka, Y. (2010). Molecular motors in neurons: transport mechanisms and roles in brain functiion, development, and disease. Neuron 68, 610-638.

Humbert, M. C., Weihbrecht, K., Searby, C. C., Li, Y., Pope, R. M., Sheffield, V. C. and Seo, S. (2012). ARL13B, PDE6D, and CEP164 form a functional network for INPP5E ciliary targeting. Proc. Natl. Acad. Sci. USA 109, 19691-19696.

Ishida, Y., Kobayashi, T., Chiba, S., Katoh, Y., and Nakayama, K. (2021). Molecular basis of ciliary defects caused by compound heterozygous IFT144/WDR19 mutations found in cranioectodermal dysplasia. Hum. Mol. Genet. 30, 213-225.

Ishikawa, H., and Marshall, W.F. (2011). Ciliogenesis: building the cell's antenna. Nat. Rev. Mol. Cell Biol. 12, 222-234.

Ismail, S. A., Chen, Y.-X., Rusinova, A., Chandra, A., Bierbaum, M., Gremer, L., Triola, G., Waldmann, H., Bastiaens, P. I. and Wittinghofer, A. (2011). Arl2-GTP and Arl3-GTP regulates a GDI-like transport system for farnesylated cargo. Nat. Chem. Biol. 7, 942-949.

Ivanova, A. A., Caspary, T., Syfriend, N. T., Duong, D. M., West, A. B., Liu, Z. and Kahn, R. A. (2017). Biochemical characterization of purified mammalian ARL13B protein indicates that it is an atypical GTPase and ARL3 guanine nucleotide exchange factor (GEF). J. Biol. Chem. 292, 11091-11108.

Jensen, V. L. and Leroux, M. R. (2017). Gates for soluble and membrane proteins, and two trafficking systems (IFT and LIFT), establish a dynamic ciliary signaling compartment. Curr. Opin. Cell Biol. 47, 83-91.

Jensen, V.L., Lambacher, N.J., Li, C., Mohan, S., Williams, C.L., Inglis, P.N., Yoder, B.K., Blacque, O.E., and Leroux, M.R. (2018). Role for intraflagellar transport in building a functional transition zone. EMBO Rep. 19, e45862.

Jordan, M.A., Diener, D.R., Stepanek, L., and Pigino, G. (2018). The cryo-EM structure

of intraflagellar transport trains reveals how dynein is inactivated to ensure unidirectional anterogarde movement in cilia. Nat. Cell Biol. 20, 1250-1255.

Katoh, Y., Chiba, S. and Nakayama, K. (2020). Practical method for superresolution imaging of primary cilia and centrioles by expansion microscopy using an amplibody for fluorescence signal amplification. Mol. Biol. Cell 31, 2195–2206.

Katoh, Y., Michisaka, S., Nozaki, S., Funabashi, T., Hirano, T., Takei, R. and Nakayama, K. (2017). Practical method for targeted disruption of cilia-related genes by using CRISPR/Cas9-mediated homology-independent knock-in system. Mol. Biol. Cell 28, 898-906.

Katoh, Y., Nakamura, K. and Nakayama, K. (2018). Visible immunoprecipitation (VIP) assay: a simple and versatile method for visual detection of protein-protein interactions. Bio-protocol 8, e2687.

Katoh, Y., Nozaki, S., Hartanto, D., Miyano, R. and Nakayama, K. (2015). Architectures of multisubunit complexes revealed by a visible immunoprecipitation assay using fluorescent fusion proteins. J. Cell Sci. 128, 2351-2362.

Katoh, Y., Terada, M., Nishijima, Y., Takei, R., Nozaki, S., Hamada, H., and Nakayama, K. (2016). Overall architecture of the intraflagellar transport (IFT)-B complex containing Cluap1/IFT38 as an essential component of the IFT-B peripheral subcomplex. J. Biol. Chem. 291, 10962-10975.

Kee, H. L., Dishinger, J. F., Blasius, T. L., Liu, C.-J., Margolis, B. and Verhey, K. J. (2012). A size-exclusion permeability barrier and nucleoporins characterize a ciliary pore complex that regulates transport into cilia. Nat. Cell Biol. 14, 431-437.

Kessler, K., Wunderlich, I., Uebe, S., Falk, N.S., Gießl, A., Brandstätter, J.H., Popp, B., Klinger, P., Ekici, A.B., Sticht, H., Dörr, H.G., Reis, A., Roepman, R., Seemanová, E., and Thiel, C.T. (2015). DYNC2LI1 mutations broaden the clinical spectrum of dynein-2 defects. Sci. Rep. 5, 11649.

Kobayashi, T., Ishida, Y., Hirano, T., Katoh, Y. and Nakayama, K. (2021). Cooperation of the IFT-A complex with the IFT-B complex is required for ciliary retrograde protein trafficking and GPCR import. Mol. Biol. Cell 32, 45-56.

Komatsu, T., Kukelyansky, I., McCaffery, J. M., Ueno, T., Varela, L. C. and Inoue, T. (2010). Organelle-specific, rapid induction of molecular activities and membrane tethering. Nat. Methods 7, 206-208.

Kong, A. M., Horan, K. A., Sriratana, A., Bailey, C. G., Collyer, L. J., Nandurkar, H. H., Shisheva, A., Layton, M. J., Rasko, J. E. J., Rowe, T. et al. (2006). Phosphatidylinositol 3-phosphate [PtdIns(3)P] is generated at the plasma membrane by an inositol polyphosphate 5-phosphatase: endogenous PtdIns(3)P can promote GLUT4 translocation to the plasma membrane. Mol. Cell. Biol. 26, 6065-6081.

Kopinke, D., Norris, A.M., and Mukhopadhyay, S. (2021). Developmental and regenerative paradigms of cilia regulated hedgehog signaling. Sem. Cell Dev. Biol. 110, 89-103.

Kösling, S. K., Fansa, E. K., Maffini, S. and Wittinghofer, A. (2018). Mechanism and

dynamics of INPP5E transport into and inside the ciliary compartment. Biol. Chem. 399, 277-292.

Lechtreck, K.-F., Brown, J. M., Sampaio, J. L., Craft, J. M., Shevchenko, A., Evans, J. E. and Witman, G. B. (2013). Cycling of the signaling protein phospholipase D through cilia requires the BBSome only for the export phase. J. Cell Biol. 201, 249-261.

Liew, G. M., Ye, F., Nager, A. R., Murphy, J. P., Lee, J. S. H., Aguiar, M., Breslow, D. K., Gygi, S. P. and Nachury, M. V. (2014). The intraflagellar transport protein IFT27 promotes BBSome exit from cilia through the GTPase ARL6/BBS3. Dev. Cell 31, 265-278.

Lin, A.E., Traum, A.Z., Sahai, I., Keppler-Noreuil, K., Kukolich, M.K., Adam, M.P., Westra, S.J., and Arts, H.H. (2013). Sensenbrenner syndrome (Cranioectodermal dysplasia): clinical and molecular analyses of 39 patients including two new patients. Am. J. Med. Genet. 161A, 2762-2776.

Lin, Y.-C., Niewiadomski, P., Lin, B., Nakamura, H., Phua, S. C., Jiao, J., Levchenko, A., Inoue, T., Rohatgi, R. and Inoue, T. (2013). Chemically inducible diffusion trap at cilia reveals molecular sieve-like barrier. Nat. Chem. Biol. 9, 437-443.

Liu, P. and Lechtreck, K. F. (2018). The Bardet-Biedl syndrome protein complex is an adaptor expanding the cargo of range of intraflagellar transport trains for ciliary export. Proc. Natl. Acad. Sci. USA 115, E934-E943.

Madhivanan, K. and Aguilar, R. C. (2014). Ciliopathies: the trafficking connection. Traffic 15, 1031-1056.

McInerney-Leo, A.M., Harris, J.E., Marshall, M.S., Gardiner, B., Kinning, E., Leong, H.Y., McKenzie, F., Ong, W.P., Vodopiutz, J., Wicking, C., Brown, M.A., Zankl, A., and Duncan, E.L. (2015). Whole exome sequencing is an efficient, sensitive and specific method for determining the genetic cause of short-rib thoracic dystrophies. Clin. Genet. 88, 550-557.

Mitchison, H.M., and Valente, E.M. (2017). Motile and non-motile cilia in human pathology: from function to phenotypes. J. Pathol. 241, 294-309.

Motohashi, K. (2015). A simple and efficient seamless DNA cloning method using SLiCE from Escherichia coli laboratory strains and its application to SLiP site-directed mutagenesis. BMC Biotechnol. 15, 47.

Mukhopadhyay, S. and Rohatgi, R. (2014). G-protein-coupled receptors, Hedgehog signaling and primary cilia. Sem. Cell Dev. Biol. 33, 63-72.

Mukhopadhyay, S., Badgandi, H.B., Hwang, S.-H., Somatilaka, B., Shimada, I.S., and Pal, K. (2017). Trafficking to the primary cilium membrane. Mol. Biol. Cell 28, 233-239.

Mukhopadhyay, S., Wen, X., Chih, B., Nelson, C. D., Lane, W. S., Scales, S. J. and Jackson, P. K. (2010). TULP3 bridges the IFT-A complex and membrane phosphoinositides to promote trafficking of G protein-coupled receptors into primary cilia. Genes Dev. 24, 2180-2193.

Nachury, M. V. and Mick, D. U. (2019). Establishing and regulating the composition of

cilia for signal transduction. Nat. Rev. Mol. Cell Biol. 20, 389-405.
Nagata, A., Hamamoto, A., Horikawa, M., Yoshimura, K., Takeda, S. and Saito, Y. (2013). Characterization of ciliary targeting sequence of rat melanin-concentrating hormone receptor 1. Gen. Comp. Endocrinol. 188, 159-165.
Nakatsu, F. (2015). A phosphoinositide code for primary cilia. Dev. Cell 34, 379-380.
Nakayama, K. and Katoh, Y. (2020). Architecture of the IFT ciliary trafficking machinery and interplay between its components. Crit. Rev. Biochem. Mol. Biol. 55, 179-196.
Nakayama, K., and Katoh, Y. (2018). Ciliary protein trafficking mediated by IFT and BBSome complexes with the aid of kinesin-2 and dynein-2 motors. J. Biochem. 163, 155-164.
Niceta, M., Margiotti, K., Digilio, M.C., Guida, V., Bruselles, A., Pizzi, S., Ferraris, A., Memo, L., Laforgia, N., Dentici, M.L., Consoli, F., Torrente, I., Ruiz-Perez, V.L., Dallapiccola, B., Marino, B., De Luca, A., and Tartaglia, M. (2018). Biallelic mutations in DYNC2LI1 are a rare cause of Ellis-van Creveld syndrome. Clin. Genet. 93, 632-639.
Nishijima, Y., Hagiya, Y., Kubo, T., Takei, R., Katoh, Y. and Nakayama, K. (2017). RABL2 interacts with the intraflagellar transport B complex and CEP19 and participates in ciliary assembly. Mol. Biol. Cell 28, 1652-1666.
Nozaki, S., Castro Araya, R. F., Katoh, Y. and Nakayama, K. (2019). Requirement of IFT-B–BBSome complex interaction in export of GPR161 from cilia. Biol. Open 8, bio043786.
Nozaki, S., Katoh, Y., Kobayashi, T. and Nakayama, K. (2018). BBS1 is involved in retrograde trafficking of ciliary GPCRs in the context of the BBSome complex. PLoS One 13, e0195005.
Nozaki, S., Katoh, Y., Terada, M., Michisaka, S., Funabashi, T., Takahashi, S., Kontani, K. and Nakayama, K. (2017). Regulation of ciliary retrograde protein trafficking by the Joubert syndrome proteins ARL13B and INPP5E. J. Cell Sci. 130, 563-576.
Okazaki, M., Kobayashi, T., Chiba, S., Takei, R., Liang, L., Nakayama, K. and Katoh, Y. (2020). Formation of the B9-domain protein complex MKS1–B9D2–B9D1 is essential as a diffusion barrier for ciliary membrane proteins. Mol. Biol. Cell 31, 2259–2268.
Parisi, M. and Glass, I. (2003 [updated 2017]). Joubert syndrome. In GeneReviews® [Internet], (eds. M. P. Adam H. H. Ardinger R. A. Pagon S. E. Wallace L. J. H. Bean K. Stephens and A. Amemiya). Seatle (WA): University of Washington.
Park, J., Lee, J., Shim, J., Han, W., Lee, J., Bae, Y. C., Chung, Y. D., Kim, C. H. and Moon, S. J. (2013). dTULP, the Drosophila melanogaster homolog of Tubby, regulates transient receptor potential channel localization in cilia. PLoS Genet. 9, e1003814.
Phua, S. C., Chiba, S., Suzuki, M., Su, E., Roberson, E. C., Pusapati, G. V., Setou, M., Rohatgi, R., Reiter, J. F., Ikegami, K. et al. (2017). Dynamic remodeling of

membrane composition drives cell cycle through primary cilia excision. Cell 168, 264-279.

Prevo, B., Scholey, J.M., and Peterman, E.J.G. (2017). Intraflagellar transport: mechanisms of motor action, cooperation, and cargo delivery. FEBS J. 284, 2905-2931.

Qiu, H., Fujisawa, S., Nozaki, S., Katoh, Y., and Nakayama, K. (2021). Interaction of INPP5E with ARL13B is essential for its ciliary membrane retention but dispensable for its ciliary entry. Biol. Open 10, bio057653.

Reiter, J. F. and Leroux, M. R. (2017). Genes and molecular pathways underpinning ciliopathies. Nat. Rev. Mol. Cell Biol. 18, 533-547.

Rosenbaum, J.L., and Witman, G.B. (2002). Intraflagellar transport. Nat. Rev. Mol. Cell Biol. 3, 813-825

Scheidel, N., and Blacque, O. (2018). Intraflagellar transport complex A genes differentially regulate cilium formation and transition zone gating. Curr. Biol. 28, 3279-3287.

Schmidts, M. (2014). Clinical genetics and pathobiology of ciliary chondrodysplasias. J. Pediatr. Genet. 3, 49-64.

Schroeder, C.M., Ostrem, J.M.L., Hertz, N.T., and Vale, R.D. (2014). A Ras-like domain in the light intermediate chain bridges the dynein motor eLife 3, e03351.

Stephen, L. A. and Ismail, S. (2016). Shuttling and sorting of lipid-modified cargo into the cilia. Biochem. Soc. Trans. 44, 1273-1280.

Sung, C.-H. and Leroux, M. R. (2013). The roles of evolutionarily conserved functional modules in cilia-related trafficking. Nat. Cell Biol. 15, 1387-1397.

Takada, N., Naito, T., Inoue, T., Nakayama, K., Takatsu, H. and Shin, H.-W. (2018). Phospholipid-flipping activity of P4-ATPase drives membrane curvature. EMBO J. 37, e97705.

Takahara, M., Katoh, Y., Nakamura, K., Hirano, T., Sugawa, M., Tsurumi, Y., and Nakayama, K. (2018). Ciliopathy-associated mutations of IFT122 impair ciliary protein trafficking but not ciliogenesis. Hum. Mol. Genet. 27, 516-528.

Takahashi, S., Kubo, K., Waguri, S., Yabashi, A., Shin, H.-W., Katoh, Y. and Nakayama, K. (2012). Rab11 regulates exocytosis of recycling vesicles at the plasma membrane. J. Cell Sci. 125, 4049-4057.

Takao, D. and Verhey, K. J. (2016). Gated entry into the ciliary compartment. Cell. Mol. Life Sci. 73, 119-127.

Taschner, M. and Lorentzen, E. (2016). The intraflagellar transport machinery. Cold Spring Harb. Perspect. Biol. 8, a028092.

Taylor, S.P., Dantas, T.J., Duran, I., Wu, S., Lachman, R.S., Consortium, U.o.W.C.f.M.G., Nelson, S.F., Cohn, D.H., Vallee, R.B., and Krakow, D. (2015). Mutations in DYNC2LI1 disrupt cilia function and cause short rib polydactyly syndrome. Nat. Commun. 6, 7092.

Thomas, S., Ritter, B., Verbich, D., Sanson, C., Bourbonnière, L., McKinney, R. A. and McPherson, P. S. (2009). Intersectin regulates dendritic spine development and

somatodendritic endocytosis but not synaptic vesicle recycling in hippocampal neurons. J. Biol. Chem. 284, 12410-12419.

Thomas, S., Wright, K. J., Le Corre, S., Micalizzi, A., Romani, M., Abhyankar, A., Saada, J., Perrault, I., Amiel, J., Litzler, J. et al. (2014). A homozygous PDE6D mutation in Joubert syndrome impairs targeting of farnesylated INPP5E protein to the primary cilium. Hum. Mut. 35, 137-146.

Toropova, K., Mladenov, K., and Roberts, A.J. (2017). Intraflagellar transport dynein is autoinhibited by trapping of its mechanical and track-binding elements. Nat. Struct. Mol. Biol. 24, 461-468.

Toropova, K., Zalyte, R., Mukhopadhyay, A.G., Mladenov, M., Carter, A.P., and Roberts, A.J. (2019). Structure of the dynein-2 complex and its assembly with intraflagellar transport trains. Nat. Struct. Mol. Biol. 26, 823-829.

Tsurumi, Y., Hamada, Y., Katoh, Y. and Nakayama, K. (2019). Interactions of the dynein-2 intermediate chain WDR34 with the light chains are required for ciliary retrograde protein trafficking. Mol. Biol. Cell 30, 658-670.

Vuolo, L., Stevenson, N.L., Heesom, K.J., and Stephens, D.J. (2018). Dynein-2 intermediate chains play crucial but distinct roles in primary cilia formation and function. eLife 7, e39655.

Vuolo, L., Stevenson, N.L., Mukhopadhyay, A.G., Roberts, A.J., and Stephens, D.J. (2020). Cytoplasmic dynein-2 at a glance. J. Cell Sci. 133, jcs240614.

Webb, S., Mukhopadhyay, A.G., and Roberts, A.J. (2020). Intraflagellar transport trains and motors: insights from structure. Sem. Cell Dev. Biol. 107, 82-90.

Ye, F., Nager, A. R. and Nachury, M. V. (2018). BBSome trains remove activated GPCRs from cilia by enabling passage through the transition zone. J. Cell Biol. 217, 1847-1868.

Zhang, Q., Giacalone, J. C., Searby, C., Stone, E. M., Tucker, B. A. and Sheffield, V. C. (2019). Disruption of RPGR protein interaction network is the common feature of RPGR variations that cause XLRP. Proc. Natl. Acad. Sci. USA 116, 1353-1360.

Zhang, Q., Li, Y., Zhang, Y., Torres, V. E., Harris, P. C., Ling, K. and Hu, J. (2016). GTP-binding of ARL-3 is activated by ARL-13 as a GEF and stabilized by UNC-119. Sci. Rep. 6, 24534.

Zhang, W., Paige Taylor, S., Ennis, H.A., Forlenza, K.N., Duran, I., Li, B., Ortiz Sanchez, J.A., Nevarez, L., Nickerson, D.A., Bamshad, M., Genomics, U.o.W.C.f.M., Lachman, R.S., Krakow, D., and Cohn, D.H. (2018). Expanding the genetic architecture and phenotypic spectrum in the skeletal ciliopathy. Hum. Mut. 39, 152-166.

Zhang, X., You, Y., Xie, X., Xu, H., Zhou, H., Lei, Y., Sun, P., Meng, Y., Wang, L., and Lu, Y. (2020). Whole-exome sequencing identified two novel mutations of DYNC2LI1 in fetal skeletal ciliopathy. Mol. Genet. Genomic Med. 8, e1524.

Zhu, X., Wang, J., Li, S., Lechtreck, K., and Pan, J. (2021). IFT54 directly interacts with kinesin-II and IFT dynein to regulate anterograde intraflagellar transport. EMBO

J. 40, e105781.